

RESEARCH

Appendix A: Supplementary Information for the Evaluation of the Delta Simulation Model-2 in Computing Tidally Driven Flows in the Sacramento–San Joaquin Delta

Vamsi K. Sridharan, Stephen G. Monimsith, Oliver B. Fringer, and Derek A. Fong

Volume 16, Issue 1 | Article 6

<https://doi.org/10.15447/sfews.2018v16iss2art6>

In this appendix, we provide the technical background for several topics on tidal hydrodynamics that appear in the main paper. We also develop the analytical basis for the 1-D parameterization of 3-D hydrodynamic processes, as well as the rationale for some of the performance metrics.

1. PHYSICAL PROCESSES IN ESTUARIES

We note that the nomenclature, notations, and conventions associated with the study of tidal flows are often esoteric or confusing. In this paper, we define the following nomenclature:

1. *transport or advection* is any physical movement of some entity with water
2. *diffusion or mixing* is the exchange of a quantity between adjacent volumes of water without any physical movement of water at a scale larger than either volume
3. *dispersion* is the spreading of a quantity as a result of various transport and mixing processes
4. *momentum* is the rate of change of energy in a water parcel, so that the transport, mixing, or dispersion of momentum indicates a redistribution of energy within a water mass

5. *scalar* is any entity such as salinity or temperature that changes the physical properties of water, or sediment or biota, which changes its quality so that the transport, mixing, or dispersion of scalars indicates a redistribution of these entities within the water mass

We also define the following nomenclature specifically for the tides:

1. *tidal components*, which are the *astronomical tidal harmonic components* or the waves of known frequencies and amplitudes that constitute the oceanic tide, and which are responsible for most tidal variations in flow and water level, as well as *overtides* caused by the interaction between the astronomical components, and *compound tides* caused by the interaction of astronomical components with mean flow, bathymetry, channel bottom friction, and junctions (Nidzieko 2010)
2. the *modulation of the subtidal flows by the tides* due to the mismatch between the incoming and outgoing tidal flows (MacCready 1999)
3. the variability in the water column depths and flows over the fortnightly *spring–neap* lunar cycle (Monismith 2016)

We also define the following notations:

1. a *tidal* quantity, ϕ , varies unsteadily over the tidal period
2. a *subtidal* quantity, $\langle\phi\rangle$, has been averaged in time over the tidal period. Here, it can refer to the riverine component of flow
3. a *cross-sectionally-averaged* quantity, $\bar{\phi}$, has been integrated over the water column
4. a quantity ϕ' *fluctuates* either about over $\langle\phi\rangle$ the tidal cycle, or about $\bar{\phi}$ across the water column
5. a quantity $\tilde{\phi}$ has been *transformed* from its original value, ϕ , by some operation

By convention,

6. the landward direction is taken as the positive streamwise or longitudinal direction, and
7. the tidal period is taken to be about 1 day, so that spring-neap tidal variations, and seasonal and inter-annual oscillations, will not be averaged by $\langle \rangle$

Unlike uni-directional flows, the tides both produce, and are influenced by, complex non-linear interactions with river flow, estuarine bathymetry, estuarine geomorphology, and other hydrodynamic inputs of energy and buoyancy. The production and influence of non-linear interactions can, at the same time, cause certain physical processes that can be very important in transporting scalars and momentum, and other physical processes that can be very important in mixing scalars and momentum. This makes the description of tidal hydrodynamics very complicated. We subsequently discuss leading-order transport processes and their associated mixing mechanisms, and then higher-order transport processes and their associated mixing mechanisms.

The tidal flow advects water over the tidal cycle in an oscillatory motion known as *tidal excursion*. This excursion interacts with the vertical and lateral shear in the water column to generate shear-induced longitudinal dispersion, which is typically half that resulting from a non-oscillatory flow of comparable amplitude (Fischer et al. 1979). This is considered to be the primary source of dispersion in long, narrow estuaries (Fischer et al. 1979). As the tides oscillate water parcels between the ocean and the estuary,

the different salinities in the two water masses and the alternate mechanisms of transporting this salinity during different tidal phases (a jet-like inflow of ocean water during the flood and a drain-like outflow of estuarine water during the ebb) result in either the net loading or unloading of salt. This phenomenon is known as *tidal pumping* (Becherer et al. 2016).

Another mechanism, *tidal trapping*—which is a subtidal circulation or differences in flow-rates between channels having different cross-sections and bottom roughnesses, or between a channel and associated shoals—occurs because of bottom roughness and bathymetric differences in multiple channels between junction sequences (Smith and Stoner 1992; Sassi et al. 2011). This can lead to the differential advection of scalars through channel networks similar to the *trapping* mechanism proposed by Okubo (1973).

A key but under-studied phenomenon in tidal systems is the so-called *tidal random walk* (Ridderinkhof and Zimmerman 1992), or the *chaotic tidal advection* of momentum and scalars through multiple channel junctions, which leads to very large or very small tidal excursions, and, consequently, enhanced longitudinal dispersion (e.g., Sassi et al. 2011; see also Sridharan 2015). This enhanced dispersion can be up to several orders of magnitude larger than the dispersion caused by conventional open-channel mechanisms (Monismith et al. 2009; Sridharan et al. 2018). These are the leading-order transport processes in tidal systems.

In addition to the leading-order mechanisms described above, tides are also involved in higher-order, but nevertheless important, subtidal flows between the estuary and the ocean. These can include both external (e.g., wind) or internal (e.g., hydraulic head) physical forcing-driven exchanges as well as density-driven exchanges. The next several paragraphs describe such physical processes.

Typically, tides in estuaries are involved in complicated subtidal flows such as (1) the exchange of water of differing salinities in different vertical layers between a river and the ocean (Geyer and MacCready 2014), (2) tidal straining or the difference in vertical shear and mixing between the ebb and flood tides, (3) stratification (Ivey et

al. 2008), (4) shoal–channel interactions, or the transfer of momentum and energy and enhanced mixing between the deep and shallow parts of an estuary (Jay et al. 1997), (5) transport and mixing resulting from the interaction of tides with residual currents induced by bathymetric and topographic variations (Geyer and Signell 1992), (6) response of the water surface of the estuary to coastal sea-level spring–neap oscillations (Monismith 2016), and (7) wind-driven circulation (Fischer et al. 1979; Csanady 1973a; Csanady 1973b; Signell et al. 1990; Monismith 2016). Together, these processes result in subtidal adjustment flows.

Wind-driven subtidal adjustment flow occurs through several mechanisms: (1) surface circulation (Fischer et al. 1979), (2) transient barotropic and baroclinic seiche (Csanady 1973a; Csanady 1973b), (3) unsteady currents from the interactions of winds and tides (Signell et al. 1990), and (4) net flows from water surface set-up by wind fetch (Monismith 2016). Of these, in the Delta, surface circulation is largely important only in open-water areas such as Suisun Bay, or flooded islands like Franks Tract, and the pumping operations forebay (MacWilliams et al. 2007); transient effects are often short-lived (Csanady 1973a); and unsteady effects can be represented with a parameterization of large bottom frictions. These mechanisms can thus be ignored in a tidal effects analysis. The water surface set-up from wind shear in the western Delta is important in the fortnightly oscillatory exchange flow (Monismith 2016) in the Delta.

Gravitational circulation is caused by density gradients from both salinity (Monismith et al. 2002) and temperature (Gleichen et al. 2014). The *gravitational circulation* induced by salinity stratification may be considered to be more important in estuaries than that induced by thermal stratification. This is because the longitudinal salinity gradient is a much stronger driver of flow than the vertical thermal stratification in typical estuaries (Geyer and MacCready 2014). Because of these considerations, the effects of thermal circulation can be ignored to first order.

In addition to subtidal adjustment flows and associated mixing mechanisms, in estuaries with branched tidal channels, the tidal signal interacts

with channel junctions to generate complex hydrodynamic signals. In particular, the beating of dominant harmonic components and their non-linear interactions produces *tidal asymmetries* or variability in the flow and water level between ebb and flood phases of tides (e.g., Woodworth et al. 2005; Nidzieko 2010). These asymmetries cause variations in sediment transport (Nidzieko 2010) and salinity intrusion (Monismith et al. 2002) over tidal phases and subtidally, and affect channel morphology (Aubrey and Speer 1984; Speer and Aubrey 1984). Moreover, flood and ebb variations in water column depth and velocity produce a net subtidal landward flux of water known as *Stokes' drift* (Longuet-Higgins 1969), which may be asymmetrically distributed at channel junctions. Stokes' drift also modifies river flow in open channels and flow splits at junctions (Sassi et al. 2011). These effects cause tide-induced variation in the subtidal flow between the ebb and flood phases.

Finally, *spring–neap variability* in the water surface elevation causes a change in the strength of cross-sectional mixing from various physical processes (MacCready and Geyer 2010). This difference in mixing modulates the subtidal adjustment flows over the spring–neap cycle in many estuaries (MacCready and Geyer 2010).

2. DERIVATIONS OF SUBTIDAL ADJUSTMENT PROCESS EXPRESSIONS

Estuarine physical processes involve the interaction of various subtidal adjustment mechanisms and subtidal flows that result from the interaction of tides with the river flow. Here, we develop the theory for some of these mechanisms supporting the descriptions in Section 3.1.

2.1. Idealized Wind-Driven Exchange Flow Resulting From Water Surface set-Up

The wind-driven exchange flow given in equation (3) is derived as follows:

Following Monismith (2016), a steady state mass balance assuming constant plan area with water column depth for the whole Delta relates filling and emptying flow from the rate of subtidal storage change as

$$Q_W \approx A_{SB} \frac{\partial \langle \eta \rangle}{\partial t} \quad (\text{A-2.1})$$

Also, the wind forcing alone captures more than 75% of the variance in the subtidal water surface set-up, which Monismith (2016) approximated from the longitudinal momentum balance over the length of Suisun Bay as

$$\Delta \langle \eta \rangle = \langle \eta_{MRZ} \rangle - \langle \eta \rangle \approx \frac{\tau_W L_{SB}}{\rho_0 g \langle H \rangle} \quad (\text{A-2.2})$$

where η_{MRZ} is the subtidal water surface elevation at Martinez, $\langle \eta \rangle$ is at the landward end of Suisun Bay, and in which the wind forces water of background density ρ_0 with a surface shear stress, τ_W given by (Fischer 1979)

$$\tau_W \approx 0.39 C_{D,W} \rho_A U_W^2 \quad (\text{A-2.3})$$

with a water-surface drag coefficient $C_{D,W}$. The factor of 0.39 is from a linear fit of wind stress to the water surface set-up in Monismith (2016).

Now, equating the rate of change of set-up over the width Suisun Bay with Q_W , and neglecting the change in $\langle \eta_{MRZ} \rangle$ as small compared to the change in set-up, and approximating the

temporal derivative as $\frac{\langle \eta \rangle_{t+1} - \langle \eta \rangle_{t-1}}{2\Delta t}$, Q_W , can be written

after algebraic manipulation as

$$Q_W \approx \left\{ \frac{C_{D,W}}{10} [Fr_{W,t+1}^2 - Fr_{W,t-1}^2] \right\} \frac{A_{SB} L_{SB}}{\Delta t} \quad (\text{A-2.4})$$

where $Fr_W = \frac{\sqrt{\langle U_W | U_W \rangle}}{\sqrt{\left(\frac{\rho_0}{\rho_A} \right) g \langle H \rangle}}$ is a water surface set-up Froude

number. Note that the sign of matches that of U_W .

2.2. Importance of Gravitational Circulation in Subtidal Adjustment

Whether an estuary is likely to be stratified, partially-mixed, or well-mixed depends on its location, its freshwater Froude number, and its estuarine mixing number (Figure 6 in Geyer and MacCready 2014). When an estuary is well-mixed, gravitational circulation is unimportant compared to tidal movements. On the other hand, in a partially-mixed

estuary, this can become important. The subsequent theory closely follows Geyer and MacCready (2014).

The freshwater Froude number is given by

$$Fr = \frac{U}{\sqrt{\gamma g S_{\text{ocean}} H}} \quad (\text{A-2.5})$$

The estuarine mixing number is given by

$$M_{\text{Mix}} = \frac{C_D U_T^2}{\omega N_0 H^2} \quad (\text{A-2.6})$$

in which $N_0 = \sqrt{\frac{\gamma g S_{\text{ocean}}}{H}}$ is the buoyancy frequency of dense seawater, and $U_T \approx \frac{|\eta|}{H} \sqrt{gH}$ is the cross-

sectionally-averaged tidal velocity (Signell et al. 1990). Typically, in dry months, U in the Sacramento River is about 0.1 ms^{-1} , and H is about 2 m. $|\eta|$ at Martinez is about 1 m, giving,

$$Fr_{\text{Dry}} \approx 0.14 \quad (\text{A-2.7})$$

$$M_{\text{Mix,Dry}} \approx 6.7$$

which indicates that the Delta could be close to well-mixed. In wet months, U in the Sacramento River is about 0.5 ms^{-1} , and is about 10 m. $|\eta|$ at Martinez is about 1 m, giving,

$$Fr_{\text{Wet}} \approx 0.31 \quad (\text{A-2.8})$$

$$M_{\text{Mix,Wet}} \approx 0.5$$

which indicates that stratification could be very important in the Delta.

2.3. Derivation of the Stokes' Drift Flow

The flow from Stokes' drift defined in Section 3.1 is given by

$$Q_{SD} = -\langle A' u'_{\eta} \rangle \quad (\text{A-2.9})$$

where A' is the area contained within the tidal range, and u'_{η} is the tidal fluctuation in the water surface velocity. The negative sign indicates that the flow is positive landward. Assuming that the cross-sectional width does not change significantly with tidal amplitude and can be represented by its RMS value, $\frac{W}{\sqrt{2}}$, and that the

flow is distributed over the water column, we can write,

$$Q_{SD} = \frac{W(h+\eta)}{\sqrt{2}} \frac{\langle \eta' u'_\eta \rangle}{h+\eta} = -\frac{A}{\sqrt{2}} \frac{\langle \eta' u'_\eta \rangle}{(h+\eta)} \quad (\text{A-2.10})$$

If we further assume that the cross-sectional velocity profile is logarithmic in the vertical and uniform laterally, then the solution of Nikuradse (Kirgöz 1989),

$$u = u_* \left[2.5 \ln \left(\frac{z}{H+\eta} \right) + 20 \right] \quad (\text{A-2.11})$$

(where u is the velocity at a point y from the channel bed and u_* is the friction velocity), can be roughness height, and nominal values of $u_* \approx 0.05 \bar{U}$, and the drag coefficient of the channel bottom, $C_D = 0.003$, have been applied.

applied at $y = H + \eta$, and integrated with respect to z , to give the water surface velocity as

$$u'_\eta = 1.1429 (\bar{U} - \langle \bar{U} \rangle) = 1.1429 \bar{U}' \quad (\text{A-2.12})$$

To get equation (A-2.10), the bed roughness height has been assumed to be approximately $\left(\frac{u_*}{\bar{U}} \right)^2 C_D H$,

which follows from equating the linearized open-channel friction force with the wall shear stress at the

3. PRESCRIPTIONS FOR MODEL RECOMMENDATIONS

We outline the alternate model grid set-ups used in Section 4.3 subsequently.

3.1. Interpolation of the Cross-Section Hydraulics for Fine-Grid Resolution

We resolve the grid as described in Section 4.3 by interpolating between existing DSM2 cross-sections. The interpolated hydraulic quantities in Figure 5 are

$$\begin{aligned} z_{0,NEW} &= \frac{Z_{0,UP} + Z_{0,DOWN}}{2}; z_{N,NEW} = \frac{Z_{N,UP} + Z_{N,DOWN}}{2} \\ z_{i,NEW} &= Z_{0,NEW} + \left(\frac{Z_{i,DOWN} - Z_{0,DOWN}}{Z_{N,DOWN} - Z_{0,DOWN}} \right) (Z_{N,NEW} - Z_{0,NEW}) \end{aligned} \quad (\text{A-3.1})$$

where $Z_{0,UP}$, $z_{0,NEW}$, $Z_{0,DOWN}$, $Z_{0,NEW}$, $z_{i,NEW}$, $Z_{i,DOWN}$, $Z_{N,UP}$, $z_{N,NEW}$, $Z_{N,DOWN}$ and are, respectively, the bottom, i^{th} intermediate, and top-most elevations of the upstream, new, and downstream cross-sections. Then,

$$W_{0,NEW} = \frac{W_{0,UP} + W_{0,DOWN}}{2}; W_{i,NEW} = \frac{W_{i,DOWN} + W_{i,UP}}{2}; W_{N,NEW} = \frac{W_{N,DOWN} + W_{N,UP}}{2} \quad (\text{A-3.2})$$

in which

$$W_{i,UP} = W_{j,UP} + \left[\frac{Z_{0,UP} + \left(\frac{z_{i,NEW} - z_{0,NEW}}{Z_{N,NEW} - Z_{0,NEW}} \right) (Z_{N,UP} - Z_{0,UP})}{Z_{j+1,UP} - Z_{j,UP}} \right] - Z_{j,UP} \left(W_{j+1,UP} - W_{j,UP} \right)$$

where $W_{0,UP}$, $W_{0,NEW}$, $W_{0,DOWN}$, $W_{i,UP}$, $W_{i,NEW}$, $W_{i,DOWN}$, $W_{N,UP}$, $W_{N,NEW}$, and $W_{N,DOWN}$ are, respectively, the bottom, i^{th} intermediate, and top-most widths of the upstream, new, and downstream cross-sections; $Z_{j,UP}$ and $Z_{j+1,UP}$ are the elevations of the j^{th} and $j+1^{\text{th}}$ points bounding the projection of the i^{th} point of the new cross-section onto the upstream cross-section; and $W_{j,UP}$ and $W_{j+1,UP}$ are the widths at these elevations of the upstream cross-section. The area and wetted perimeter are now given by

$$A_{i,NEW} = \sum_{k=1}^i \frac{(W_{k,NEW} + W_{k-1,NEW})}{2} (Z_{k,NEW} - Z_{k-1,NEW}); A_{0,NEW} = 0 \quad (A-3.3)$$

$$WP_{i,NEW} = W_{0,NEW} + 2 \sum_{k=1}^i \sqrt{\left(\frac{W_{k,NEW} - W_{k-1,NEW}}{2} \right)^2 + (Z_{k,NEW} - Z_{k-1,NEW})^2}$$

where $A_{i,NEW}$ and $A_{0,NEW}$ are the cross-sectional areas at the bottom and i^{th} elevation, and $WP_{i,NEW}$ and $WP_{0,NEW}$ are the wetted perimeters at the bottom and i^{th} elevation. Here k is the summation index from the channel bottom to the i^{th} elevation.

3.2 Idealized Shoal–Channel Prescriptions

Here, we describe an idealized representation of a shoal–channel system within the DSM2 framework (Figure 4). As a consequence, the problem of negative rate of change of conveyance with rapidly varying cross-sections discussed in Sections 6.1 and 6.2 is also eliminated.

We idealized the processes described in Section 3.1 (Figures 4A, 4B) by a network of three prismatic rectangular channels in parallel, of which the middle channel is deep and smooth, and the side channels are shallow, wide, and rough (Figures 4C, 4D). After Ralston and Stacey (2005), the system is 10 km long with a bottom slope of 0.0005, a 50-m-wide and 2-m-deep main channel, and 375-m-wide and 1-m-deep shoals. The shoals and channel are broken into reaches connected by DSM2 nodes every 500 m to facilitate mixing and water surface equalization (Figure 4C). The water flows freely in all the channels during the flood phase of the tide (Figure 4D). Caissons at the ends of each channel that represent shoals are set to close when the water column depth is likely to fall below a threshold value of 30 mm above the highest bed elevation in a channel reach (red gates in Figure 4C). This prevents further drainage of water into the channel, and simulates drying.

We investigated two hydrodynamic settings to simulate shoal–channel exchange, and wetting and drying. For the shoal–channel exchange case, we set the Manning's n for the main channel to a typical open-channel value of 0.01, and for the shoals to a typical floodplain value of 0.1 (Furniss et al. 2006). A single value of the integral length scale for longitudinal dispersion was specified for

all three DSM2 channels using equation (8) in which $K \approx 30 \text{ m}^2 \text{ s}^{-1}$ (see Table 1 in Ralston and Stacey [2005]) and $U \approx 0.3 \text{ m s}^{-1}$ (Ralston and Stacey 2005) to give $l_f = 100 \text{ m}$. The system has an initial water column depth of 1.5 m and is forced at the ocean end by an M_2 tide of 0.75 m amplitude and salinity of 28 psu (Ralston and Stacey 2005). To simulate the upstream freshwater flow, we added a nominal river flow of $28.3 \text{ m}^3 \text{ s}^{-1}$ with a salinity of 5 psu. As Qual computes only the electrical conductivity, we converted the salinity to electrical conductivity using the simplified conversion formula given by Schemel (2001) as

$$C = J_0 S + S(S - 35) \left(J_1 + J_2 \sqrt{S} + J_3 S + J_4 S^{2/3} \right) \quad (A-3.4)$$

where S is the salinity in the psu scale and

$J_0 = 1516.8$, $J_1 = -16.072$, $J_2 = 4.1495$, $J_3 = -0.5345$, and $J_4 = 0.0261$ are constants at a reference temperature of 25 °C. To compare model results to those reported in Ralston and Stacey, we converted electrical conductivity back to salinity

$$S = K_0 + K_1 \sqrt{\left(\frac{C}{C_0} \right)} + K_2 \left(\frac{C}{C_0} \right) + K_3 \left(\frac{C}{C_0} \right)^{3/2} + K_4 \left(\frac{C}{C_0} \right)^2 + K_5 \left(\frac{C}{C_0} \right)^{5/2} \quad (A-3.5)$$

where C_0 is the specific conductance of

$53.087 \text{ mS cm}^{-1}$ at 25 °C, and $K_0 = 0.012$, $K_1 = -0.2174$, $K_2 = 25.3283$, $K_3 = 13.7714$, $K_4 = -6.4788$, and $K_5 = 2.5842$ are constants.

To simulate the wetting and drying problem, we set the Manning's n for the main channel and shoals to more comparable values of 0.02 and 0.035, respectively (Furniss et al. 2006). We forced the model with an M_2 tide of 1.5 m amplitude and an upstream river flow of $4.5 \text{ m}^3 \text{ s}^{-1}$.

To demonstrate that such a model would also eliminate the negative rate of change of conveyance problem in rapidly varying cross-sections, consider the following: Suppose there exists a shoal-channel cross-section with main-channel bottom width of 100 m, depth of 1.5 m, main-channel side slope of 1, and shoal slope of 0.001, and suppose the water level varies from 1 m to 1.5 m to 1.9 m in three time-steps. A typical DSM2 computation would result in the hydraulic parameters listed in Table A-3.1. Note the rapid change in wetted perimeter, hydraulic radius, and the negative rate of change of conveyance with water column depth. Alternately, if we prescribe this cross-section as two adjacent parallel channels with a shoal represented by a large Manning's value, we would have Table A-3.2. Observe now that the changes in hydraulic parameters are more gradual in the main channel, and that there is no negative rate

of change of conveyance with water column depth. More important, because the conveyance in the shoal is negligible compared to that in the main channel, modeling the tidal dynamics will not be adversely affected.

3.3 Carquinez Strait Extension

To extend the grid to include Carquinez Strait, we (1) extracted the bathymetry of Carquinez Strait from the 10-m Digital Elevation Map (DEM) of the Delta (Wang and Ateljevich 2012) using QGIS (QGIS Development Team 2016) (Figure 6A); (2) digitized the thalweg, or centerline, of the channel and transformed the Universal Transverse Mercator coordinates of the bathymetry points to a coordinate system aligned with the thalweg by applying the algorithm in Merwade et al. (2005) using the MATLAB *xy2sn* toolbox (Dugge c2015); (3) longitudinally averaged the cross-sectional bathymetry over 1.5- to 3.5-km-long reaches in which the channel was relatively uniform; and (4) extracted representative DSM2 cross-sections according to the guidelines of the Cross Section Development Program (Finch et al. 2001) in MATLAB (Figure 4A). The resulting channel was 9.3 km long and had four cross-sections (Figures 6B–6E). We assigned the Manning's and integral mixing length scale values between Port Chicago and Martinez to Carquinez Strait.

Table A-3.1 Hydraulic properties in channel cross-section at subsequent time-steps

Hydraulic parameter	Time step 1	Time step 2	Time step 3
Depth (m)	1	1.5	1.9
Side slope	1	1	0.001
Manning's	0.01	0.01	0.01
Wetted perimeter (m)	102.8	104.2	504.8
Area (m ²)	101	152.3	273.3
Hydraulic radius (m)	0.98	1.46	0.54
Conveyance (m ³ s ⁻¹)	14870	29202	27055
dConveyance/dz (m ³ s ⁻¹)	28665	-5368.5	

Table A-3.2 Hydraulic properties in shoal-channel cross-sections at subsequent time-steps

Hydraulic parameter	Time step 1 in main channel	Time step 2 in main channel	Time step 3 in main channel	Time step 3 in shoal
Depth (m)	1	1.5	1.9	0.4
Side slope	1	1	1	0.001
Manning's	0.01	0.01	0.01	1
Wetted perimeter (m)	102.8	104.2	105.2	400.4
Area (m ²)	101	152.3	192.9	80.5
Hydraulic radius (m)	0.98	1.46	1.83	0.2
Conveyance (m ³ s ⁻¹)	14870	29202	43038	41.2
dConveyance/dz (m ³ s ⁻¹)		28665	34589	41.2

4. DATA SOURCES AND QUALITY CONTROL

We collected water level, flow, and electrical conductivity data from 93 locations within the Delta from the CDEC data base (CDEC c2016). The data typically spans the period between 1 October 2008 and 30 September 2015.

4.1 Data Sources and Quality Control

We subjected the data we collected to rigorous quality control using the MATLAB-based KATANA toolbox (V.K. Sridharan 2018, unreferenced, see “Notes”).

Briefly, the toolbox corrected poorly interpolated and noisy data, erroneous outliers, and instrumentation bias such as spurious jumps, drifts, spikes, and modulations in the true signal. Signal clean-up involved multiple water levels. The correlation in the spectrogram between two nearby stations was initially used to quantify and remove river influence in the signal. After this, thresholds were imposed on higher-order temporal derivatives of the signal to remove gross interpolations and noise-saturated signal chunks, followed by a moving median threshold to remove outliers. Then the surviving signal was filtered into tidal, subtidal, and long-period components, and the long-period component was subject to a maximal overlap discrete wavelet transformation (Cornish et al. 2006), in which the transform coefficients corresponding to multi-scale edge features were removed (Patel et al. 2014). Subsequently, to correct spurious amplitude modulations and sudden biases, local information in the subtidal and tidal components was compared relative to the whole signal. Consequently, these components were added to recover the uncorrupted signal. To facilitate a direct comparison between water level measurements referenced to different elevations, and the DSM2 water levels referenced to the NAVD88, we corrected all observed water column depths by subtracting the datum correction values specified in [Tables A-4.1 to A-4.12](#).

4.2 Continuous Monitoring Stations in the Delta

The details of the data records are presented in [Tables A-4.1 to A-4.12](#). In each table, footnotes indicate the following:

- a. Refer to the CDWR DSM2 grid (BDO c2002) for exact locations of the nodes.
- b. Indicates the data used from a location, i.e., water level (ft.), flow (cfs), and/or electrical conductivity ($\mu\text{S}/\text{cm}$), respectively.
- c. Indicates the collection methods for water level, flow, and electrical conductivity, respectively. Here, because further clarification is not provided in the CDEC data base, measured flow could indicate either by ADCP or by current meter; measured electrical conductivity could indicate either by in situ meter, microwave emittance or satellite refractivity; and estimated electrical conductivity indicates any indirect estimation technique.
- d. Indicates the data reporting frequency for water level, flow, and electrical conductivity respectively. One hour indicates continuous data, and 15 minutes indicates triggered measurements.
- e. Indicates the difference in datum between measured and modeled water levels.

4.3 Data Precision

In reporting all our results, we assumed the CDEC data to have a precision in water level measurements of (1) $\pm 3\%$ of the tidal range by microwave sensor (Park et al. 2014), (2) $\pm 0.1\text{ m}$ conservatively by satellite altimetry (Calmant and Seyler 2006), and (3) $\pm 0.003\text{ m}$ by stream gage (USGS c2016), and a precision in flow measurement of $\pm 5\%$ conservatively by ADCP (Muste et al. 2004) and by rating curves (Braca 2008). The NOAA-TC and RTC buoy data have precisions of $\pm 0.03\text{ m}$ (NOAA-TC c2013; RTC c2017). Because no information about the precision of the electrical conductivity measurements was available, we assumed a typical precision for electrical conductivity log gers of $\pm 5\%$ of the reported value when the electrical conductivity was lower than $10,000\mu\text{S cm}^{-1}$ and $\pm 15\%$ when it exceeded this threshold (e.g., Onset 2017). We report the model results also to the CDEC precision for the model configurations, G*T*B1, and to the NOAA-TC and

Table A-4.1 Description of observations in the Sacramento River

Station	Station code	Nearest DSM2 node ^a	Data source	Data ^b	Collection method ^c	Frequency ^d	Datum correction for DSM2 comparison (m) ^e
Sacramento River at I Street Bridge	IST	330	CDWR-NCRO	Water level	Satellite altimetry	1 hour	−5.04
Sacramento River at Freeport	FPT	RSAC155	USGS	Water level	Satellite altimetry	1 hour	23.13
				Flow	Rating curve	1 hour	
Sacramento River at Hood	SRH	RSAC142	CDWR-DES	Electrical conductivity	Measured	1 hour	NA
Sacramento River above Delta Cross Channel	SDC	RSAC128	USGS	Water level	Stream gauge	1 hour	−8.67
				Flow	Measured	1 hour	
Sacramento River below Georgiana Slough	GES	Between 343 and 344	USGS	Water level	Satellite altimetry	15 minutes	−9.94
				Flow	Measured	15 minutes	
				Electrical conductivity	Measured	15 minutes	
Sacramento River at Rio Vista Bridge	RVB	RSAC101	CDWR-DES	Water level	Stream gauge	1 hour	−14.17
	SRV			Flow	Measured	1 hour	
	RIV			Electrical conductivity	Measured	1 hour	
Sacramento River at Decker Island	SDI	Between 352 and 353	USGS	Electrical conductivity	Measured	15 minutes	NA
Emmaton	EMM	RSAC092	USBR	Electrical conductivity	Measured	1 hour	NA
Collinsville on Sacramento River	CSE	RSAC081	CDWR-DES	Water level	Satellite altimetry	1 hour	−12.13
				Electrical conductivity	Measured	1 hour	

Table A-4.2 Description of observations in Sutter and Steamboat sloughs

Station	Station code	Nearest DSM2 node ^a	Data source	Data ^b	Collection method ^c	Frequency ^d	Datum correction for DSM2 comparison (m) ^e
Sutter Slough at Courtland	SUT	Between 339 and 300	USGS	Water level	Satellite altimetry	15 minutes	−6.48
				Flow	Measured	15 minutes	
				Electrical conductivity	Measured	15 minutes	
Steamboat Slough between Sacramento River and Sutter Slough	SSS	Between 340 and 303	USGS	Water level	Satellite altimetry	15 minutes	−3.31
				Flow	Measured	15 minutes	
				Electrical conductivity	Measured	15 minutes	
Miner Slough at Highway 84 Bridge	HWB	Between 302 and 307	USGS	Water level	Satellite altimetry	15 minutes	−5.00
				Flow	Measured	15 minutes	
				Electrical conductivity	Measured	15 minutes	
Miner Slough at Five Points	MFV	316	CDWR-NCRO	Water level	Satellite altimetry	15 minutes	−5.18
Sacramento Deep Water Shipping Channel	DWS	Between 315 and 316	USGS	Water level	Satellite altimetry	15 minutes	−0.80
				Flow	Measured	15 minutes	
				Electrical conductivity	Measured	15 minutes	
Cache Slough at Ryer Island	RYI	Between 316 and 350	USGS	Water level	Satellite altimetry	15 minutes	−13.20
				Flow	Measured	15 minutes	
				Electrical conductivity	Measured	15 minutes	

Table A-4.3 Description of observations in Georgiana Slough

Station	Station code	Nearest DSM2 node ^a	Data source	Data ^b	Collection method ^c	Frequency ^d	Datum correction for DSM2 comparison (m) ^e
Georgiana Slough at Sacramento River	GSS	Between 343 and 288	USGS	Water level	Satellite altimetry	15 minutes	-5.11
				Flow	Measured	15 minutes	
				Electrical conductivity	Measured	15 minutes	

Table A-4.4 Description of observations in the South Fork Mokelumne River

Station	Station code	Nearest DSM2 node ^a	Data source	Data ^b	Collection method ^c	Frequency ^d	Datum correction for DSM2 comparison (m) ^e
Delta Cross Channel between Sacramento River and Snodgrass	DLC	Between 342 and 255	USGS	Water level	Satellite altimetry	15 minutes	-4.66
				Flow	Measured	15 minutes	
				Electrical conductivity	Measured	15 minutes	
North Mokelumne River at West Walnut Grove Road	NMR	RMKL019	USGS	Water level	Satellite altimetry	15 minutes	-2.84
				Flow	Measured	15 minutes	
				Electrical conductivity	Measured	15 minutes	
South Mokelumne River at West Walnut Grove Road	SMR	RSMKL024	USGS	Water level	Satellite altimetry	15 minutes	-2.71
				Flow	Measured	15 minutes	
				Electrical conductivity	Measured	15 minutes	
Staten Island	STI	RSMKL008	USBR	Electrical conductivity	Measured	1 hour	NA
Little Potato Slough at Terminous	LPS	Between 249 and 250	USGS	Water level	Satellite altimetry	15 minutes	-3.72
				Flow	Measured	15 minutes	
				Electrical conductivity	Measured	15 minutes	
Mokelumne River at San Joaquin River	MOK	Between 272 and 40	USGS/CDWR	Water level	Satellite altimetry	15 minutes	-8.50
				Flow	Measured	15 minutes	
				Electrical conductivity	Measured	15 minutes	

Table A-4.5 Description of observations in Yolo Bypass

Station	Station code	Nearest DSM2 node ^a	Data source	Data ^b	Collection method ^c	Frequency ^d	Datum correction for DSM2 comparison (m) ^e
Yolo Bypass at Lisbon	LIS	CHSAC031	CDWR	Water level	Satellite altimetry	1 hour	-10.29
				Flow	Measured	1 hour	
				Electrical conductivity	Measured	15 minutes	
Liberty Island at approximate center of South End	LIB	Between 322 and 323	USGS	Water level	Satellite altimetry	15 minutes	-7.24
				Flow	Measured	15 minutes	
				Electrical conductivity	Measured	15 minutes	

Table A-4.6 Description of observations in Suisun Bay

Station	Station code	Nearest DSM2 node ^a	Data source	Data ^b	Collection method ^c	Frequency ^d	Datum correction for DSM2 comparison (m) ^e
Sacramento River at Mallard Island	MAL	RSAC075	CDWR-DES	Electrical conductivity	Measured	1 hour	NA
Port Chicago	PCT	RSAC064	USBR	Electrical conductivity	Measured	1 hour	NA

Table A-4.7 Description of observations in Suisun Marsh

Station	Station code	Nearest DSM2 node ^a	Data source	Data ^b	Collection method ^c	Frequency ^d	Datum correction for DSM2 comparison (m) ^e
Roaring River	ROR	Between 432 and 418	CDWR-DES	Water level	Satellite altimetry	1 hour	-1.93
				Electrical conductivity	Measured	15 minutes	
Montezuma Slough at Roaring River	MSL	418	CDWR-DES	Water level	Satellite altimetry	1 hour	-6.28
				Electrical conductivity	Measured	1 hour	
National Steel	NSL	SLMZU025	CDWR-DES	Water level	Satellite altimetry	1 hour	-5.30
				Electrical conductivity	Measured	1 hour	
Beldon Landing	BDL	SLMZU011	CDWR-DES	Water level	Satellite altimetry	15 minutes	-7.55
				Electrical conductivity	Measured	15 minutes	
Hunter Cut at Montezuma Slough	HUN	SLMZU003	CDWR-DES	Water level	Satellite altimetry	15 minutes	-6.95
				Electrical conductivity	Measured	15 minutes	
Godfather Island on Suisun Slough	GOD	Between 377 and 378	CDWR-DES	Electrical conductivity	Measured	1 hour	NA
Goodyear Slough outfall at Naval Fleet	FLT	SLGYR008	CDWR-DES	Electrical conductivity	Measured	15 minutes	NA

Table A-4.8 Description of observations in Carquinez Strait

Station	Station code	Nearest DSM2 node ^a	Data source	Data ^b	Collection method ^c	Frequency ^d	Datum correction for DSM2 comparison (m) ^e
Martinez	MRZ	RSAC054	CDWR-DES	Water level	Stream gauge	1 hour	-15.96
				Electrical conductivity	Measured	1 hour	
Martinez at Amorco Pier	MAP	RSAC054	NOAA-NDBC	Water level	Tide gauge	6 minutes	-16.81
Carquinez Strait	CAR	Downstream of RSAC054	RTC	Water level	Pressure transducer	6 minutes	-0.715

Table A-4.9 Description of observations in the flooded islands

Station	Station code	Nearest DSM2 node ^a	Data source	Data ^b	Collection method ^c	Frequency ^d	Datum correction for DSM2 comparison (m) ^e
Dutch Slough at Jersey Island	DSJ	SLDUT007	USGS	Water level	Satellite Altimetry	15 minutes	-3.68
				Flow	Measured	15 minutes	
				Electrical conductivity	Measured	15 minutes	
False River near Oakley	FAL	Between 226 and 44	USGS/CDWR	Water level	Satellite altimetry	15 minutes	-6.87
				Flow	Measured	15 minutes	
				Electrical conductivity	Measured	15 minutes	
Farrar Park	FRP	SLDUT009	USBR	Electrical conductivity	Measured	1 hour	NA
Bethel Island	BET	SLPPR003	CDWR	Electrical conductivity	Measured	1 hour	NA
Discovery Bay at Indian Slough	DBI	Between 196 and 197	CDWR	Water level	Rating curve	15 minutes	-4.92
Turner Cut near Holt	TRN	Between 140 and 26	USGS/CDWR	Water level	Satellite altimetry	15 minutes	-4.36
				Flow	Measured	15 minutes	
				Electrical conductivity	Measured	15 minutes	

Table A-4.10 Description of observations in the canals

Station	Station code	Nearest DSM2 node ^a	Data source	Data ^b	Collection method ^c	Frequency ^d	Datum correction for DSM2 comparison (m) ^e
West Canal at Clifton Court Intake	WCI	Between 72 and 182	CDWR-NCRO	Flow	Measured	15 minutes	NA
Victoria Canal near Byron	VCU	CHVCT000	USGS/DWR	Water level	Satellite altimetry	15 minutes	-2.00
				Flow	Measured	15 minutes	
				Electrical conductivity	Measured	15 minutes	
Middle River at Union Point	MUP	Between 113 and 188	CDWR-NCRO	Electrical conductivity	Measured	15 minutes	NA
Grant Line Canal	GLC	Between 178 and 71	USGS/CDWR	Water level	Stream gauge	1 hour	-4.19
				Flow	Measured	1 hour	
				Electrical conductivity	Estimated	1 hour	
Grant Line Canal at Tracy Road Bridge	GCT	CHGRL009	CDWR	Water level	Satellite altimetry	1 hour	-5.05
				Electrical conductivity	Measured	15 minutes	
Grant Line Canal East	GLE	Between 171 and 172	CDWR-NCRO	Flow	Measured	15 minutes	NA
				Electrical conductivity	Measured	15 minutes	

Table A-4.11 Description of observations in the Old and Middle rivers

Station	Station code	Nearest DSM2 node ^a	Data source	Data ^b	Collection method ^c	Frequency ^d	Datum correction for DSM2 comparison (m) ^e
Old River at Frank's Tract near Terminous	OSJ	Between 103 and 38	USGS/CDWR	Water level	Satellite altimetry	1 hour	-8.42
				Flow	Measured	15 minutes	
				Electrical conductivity	Measured	1 hour	
Old River at Quimby Island near Bethel Island	ORQ	Between 100 and 101	USGS/CDWR	Water level	Satellite altimetry	15 minutes	-9.24
				Flow	Measured	15 minutes	
				Electrical conductivity	Measured	15 minutes	
Holland Cut near Bethel Island	HOL	Between 99 and 102	USGS/CDWR	Water level	Satellite altimetry	15 minutes	-5.46
				Flow	Measured	15 minutes	
				Electrical conductivity	Measured	15 minutes	
Middle River near Holt	HLT	Between 130 and 131	USGS/CDWR	Water level	Satellite altimetry	15 minutes	-5.55
				Electrical conductivity	Measured	15 minutes	
Holland Tract	HLL	ROLD014	USBR	Electrical conductivity	Measured	1 hour	NA
Old and Middle Rivers tidally filtered estimate	OMR	ROLD034 and RMID015	CDWR-NCRO	Flow	Computed by filtering OH4+MDM	1 hour	NA
Old River at Bacon Island	OBI	ROLD024	USGS/DWR	Water level	Satellite altimetry	1 hour	-8.32
				Flow	Measured	1 hour	
				Electrical conductivity	Measured	1 hour	
Middle River at Middle River	MDM	RMID015	USGS	Water level	Satellite altimetry	1 hour	-8.72
				Flow	Measured	1 hour	
				Electrical conductivity	Measured	1 hour	
Jones Tract	JTR	Between 117 and 118	CDWR-NCRO	Water level	Satellite altimetry	15 minutes	-7.07
				Flow	Rating curve	15 minutes	
Old River at Byron	ORB	ROLD034	CDWR	Water level	Rating curve	15 minutes	-6.92
Old River at Highway 4	OH4	ROLD034	USGS	Water level	Satellite altimetry	1 hour	-6.91
				Flow	Measured	1 hour	
				Electrical conductivity	Measured	1 hour	
Old River at Coney Island	CIS	Between 183 and 185	CDWR	Water level	Satellite altimetry	15 minutes	-2.79
Old River at Clifton Court Intake	ORI	Between 71 and 72	CDWR-NCRO	Flow	Measured	15 minutes	NA
Old River near Delta Mendota Canal below dam	OBD	ROLD046	CDWR	Water level	Satellite altimetry	15 minutes	-2.37
				Electrical conductivity	Measured	15 minutes	

Table A-4.11 Description of observations in the Old and Middle rivers (continued)

Station	Station code	Nearest DSM2 node ^a	Data source	Data ^b	Collection method ^c	Frequency ^d	Datum correction for DSM2 comparison (m) ^e
Old River at Delta Mendota Canal	ODM	69	USGS/CDWR	Water level	Satellite altimetry	15 minutes	-2.44
				Flow	Rating curve	15 minutes	
				Electrical conductivity	Measured	15 minutes	
Old River at Tracy Wildlife Association	TWA	61	CDWR-NCRO	Electrical conductivity	Measured	15 minutes	NA
Old River near Tracy	OLD	ROLD059	CDWR-O&M	Water level	Rating curve	15 minutes	-2.16
				Flow	Measured	15 minutes	
				Electrical conductivity	Measured	15 minutes	
Old River above Doughty Cut	ORX	Between 53 and 54	CDWR-NCRO	Flow	Measured	15 minutes	NA
				Electrical conductivity	Measured	15 minutes	
Doughty Cut above Grant Line Canal	DGL	Between 56 and 171	CDWR	Water level	Satellite altimetry	1 hour	-3.23
				Electrical conductivity	Measured	15 minutes	
Victoria Island	VIC	RMID023	USBR	Electrical conductivity	Measured	1 hour	NA
Middle River above barrier	MAB	Between 112 and 113	CDWR-NCRO	Flow	Measured	15 minutes	NA
Middle River at Tracy Boulevard	MTB	RMID027	CDWR	Water level	Rating curve	15 minutes	-1.84
				Electrical conductivity	Measured	15 minutes	
Middle River at Howard Road Bridge	MHR	Between 107 and 108	CDWR	Water level	Satellite altimetry	15 minutes	-0.82
				Electrical conductivity	Measured	15 minutes	
Middle River near Howard Road Bridge	MHO	107	CDWR-NCRO	Electrical conductivity	Measured	15 minutes	NA
Middle River at Undine Road	MRU	RMID040	CDWR-NCRO	Flow	Measured	15 minutes	NA
				Electrical conductivity	Measured	15 minutes	
Union Island	UNI	RMID041	USBR	Electrical conductivity	Measured	1 hour	NA
Old River at Head	OH1	ROLD074	CDWR	Water level	Rating curve	1 hour	-3.30
				Flow	Rating curve	1 hour	
				Electrical conductivity	Measured	15 minutes	

Table A-4.12 Description of observations in the San Joaquin River

Station	Station code	Nearest DSM2 node ^a	Data source	Data ^b	Collection method ^c	Frequency ^d	Datum correction for DSM2 comparison (m) ^e
Pittsburg	PTS	Between 463 and 356	USBR	Electrical conductivity	Measured	1 hour	NA
Antioch	ANH	RSAN007	CDWR-DES	Water level	Satellite altimetry	1 hour	-11.93
				Electrical conductivity	Measured	1 hour	
Blind Point	BLP	RSAN014	CDWR	Electrical conductivity	Measured	15 minutes	NA
San Joaquin River at Jersey Point	SJJ	RSAN018	USGS	Water level	Satellite altimetry	15 minutes	-12.85
				Flow	Measured	15 minutes	
				Electrical conductivity	Measured	15 minutes	
Three Mile Slough	TMS	Between 240 and 352	CDWR	Electrical conductivity	Measured	15 minutes	NA
Three Mile Slough at San Joaquin River	TSL	Between SLTRM004 and 240	USGS/CDWR	Water level	Satellite altimetry	15 minutes	-6.77
				Flow	Measured	15 minutes	
				Electrical conductivity	Measured	15 minutes	
San Andreas Landing	SAL	RSAN032	USBR	Electrical conductivity	Measured	1 hour	NA
Prisoner's Point	PPT	Between 37 and 38	CDWR-DES	Electrical conductivity	Estimated	1 hour	NA
San Joaquin River at Prisoner's Point near Terminus	PRI	RSAN037	USGS	Water level	Satellite altimetry	15 minutes	-13.53
				Flow	Measured	15 minutes	
				Electrical conductivity	Measured	15 minutes	
San Joaquin River at Venice Island	VNI	RSAN043	CDWR-O&M	Water level	Satellite altimetry	15 minutes	-5.82
San Joaquin River at Garwood Bridge	SJG	Between 14 and 15	USGS	Water level	Satellite altimetry	15 minutes	-3.76
				Flow	Measured	15 minutes	
				Electrical conductivity	Measured	15 minutes	
San Joaquin River at Brandt Bridge	BDT	RSAN072	CDWR-O&M	Water level	Satellite altimetry	15 minutes	-2.57
				Flow	Measured	15 minutes	
				Electrical conductivity	Measured	15 minutes	
San Joaquin River above Dos Reis	SJD	Between 8 and 9	CDWR-NCRO	Flow	Measured	15 minutes	NA
				Electrical conductivity	Measured	15 minutes	
San Joaquin River below Old River near Lathrop	SJL	Between 8 and 9	CDWR	Water level	Satellite altimetry	15 minutes	-2.17
				Electrical conductivity	Measured	15 minutes	

Table A-4.12 Description of observations in the San Joaquin River (continued)

Station	Station code	Nearest DSM2 node ^a	Data source	Data ^b	Collection method ^c	Frequency ^d	Datum correction for DSM2 comparison (m) ^e
San Joaquin River at Mossdale Bridge	MSD	RSAN087	CDWR-DES	Water level	Rating curve	15 minutes	-1.81
				Flow	Measured	15 minutes	
				Electrical conductivity	Measured	15 minutes	
New Jerusalem drain	NJD	4	Univ. Pacific	Electrical conductivity	Measured	15 minutes	-2.19
San Joaquin River McCune station near Vernalis	SJR	Between 1 and 2	CDWR-DES	Electrical conductivity	Measured	1 hour	NA
San Joaquin River near Vernalis	VNS	RSAN112	USGS/CDWR	Water level	Stream gauge	1 hour	0.77
				Flow	Rating curve	1 hour	

RTC buoy precision for the model configurations, G*T*B2 and G*T*BB. We report the DAYFLOW $\widehat{\text{NDOI}}$ estimate and the model results to the nearest whole numbers, because DAYFLOW is known to be imprecise at low flow-rates (Monismith et al. 2002).

5. PRESCRIPTIONS FOR COMPARISON WITH DATA AND INTER-MODEL COMPARISON

We detail the assumptions inherent to the model-data comparisons, and the various metrics listed in Section 4.5 subsequently.

5.1 DAYFLOW NDOI and Observed OMR Flow

The is a DAYFLOW-estimated parameter that does not account for tidal variations and the fortnightly variation in Delta storage (Monismith 2016). For the comparison between the and the model results to be fair, the effect of subtidal adjustment must be subtracted from the (see Section 3.1). Here, we removed the coastal ocean oscillation, wind- and density-driven components of the subtidal estuarine adjustment through the use of the simple parameterizations in equations (3) and (4). To account for the subtidal adjustment flows, we compared the modeled defined as

$$Q_{\text{NDOI}} = \langle Q_{\text{SRV}} + Q_{\text{TSL}} + Q_{\text{SJJ}} + Q_{\text{DSJ}} \rangle \quad (\text{A-5.1})$$

where Q_{SRV} , Q_{TSL} , Q_{SJJ} , and Q_{DSJ} are, respectively, the flows at Rio Vista, Threemile Slough, Jersey Point, and Dutch Slough (Figure 1; DWR c2016), with a modified DAYFLOW NDOI as

$$\widehat{\text{NDOI}} = \text{NDOI} - (Q_w + Q_s) \quad (\text{A-5.2})$$

where the subtidal adjustment flow is positive directed oceanward. We also compared the observed and modeled flow, defined as

$$Q_{\text{OMR}} = \langle Q_{\text{OH4}} + Q_{\text{MDM}} \rangle \quad (\text{A-5.3})$$

where Q_{OH4} and Q_{MDM} are, respectively, the flows in the Old River at Highway 4 and in the Middle River.

5.2 Aggregate Performance Metric

To overcome the challenges listed in Section 4.5, we developed and . To estimate these quantities, we first assigned equal weightage for the model's ability to predict flow and water column depth, because these are both equally important hydrodynamic quantities. Then, we required that the contribution to the aggregate model error at a particular location be weighted by a measure of how correlated the data at that location is to data at other locations. So, for instance, if there are several locations in the OMR corridor where flow is measured and over which the flow is well correlated, and only a few locations in the Sacramento River, then the contribution of error

from locations in the Sacramento River must be weighted higher than the contributions from OMR.

We defined ε_{Σ} and MSS_{Σ} as

$$\varepsilon_{\Sigma,p} = \sum_{\phi \in \{H,Q\}} \left[\frac{\sum_{i=1}^{N_{\phi}} \left(\frac{\varepsilon_{\phi,p,i}^2}{N_{\phi,i}} \right)}{\sum_{i=1}^{N_{\phi}} \left(\frac{\phi_{0,i}^2}{N_{\phi,i}} \right)} \right] \quad (\text{A-5.4})$$

$$\begin{aligned} \varepsilon_{\phi,p,i}^2 &= \sum_{j=1}^{N_i} \left(\phi_{M,p,i,j} - \phi_{0,i,j} \right)^2 \\ \phi_{0,i}^2 &= \sum_{j=1}^{N_i} \phi_{0,i,j}^2 \end{aligned}$$

$$MSS_{\Sigma,p} = 1 - \frac{1}{2} \sum_{\phi \in \{H,Q\}} \left[\frac{\sum_{i=1}^{N_{\phi}} \left(\frac{\varepsilon_{\phi,p,i}^2}{N_{\phi,i}} \right)}{\sum_{i=1}^{N_{\phi}} \left(\frac{PE_{\phi,p,i}^2}{N_{\phi,i}} \right)} \right] \quad (\text{A-5.5})$$

$$PE_{\phi,p,i} = \sum_{j=1}^{N_i} \left(\left| \phi_{M,p,j}^{(i)} - \overline{\phi_0^{(i)}} \right| + \left| \phi_{M,p,j}^{(i)} - \overline{\phi_0^{(l)}} \right| \right)^2$$

where, for a model configuration, p , the contributions to the cumulative squared error, $\varepsilon_{\phi,p}^2$, in ϕ by a location, i , are weighted by the reciprocal of the number of locations at which observations are correlated with this those at this location, $N_{\phi,i}$, and summed over all locations where such measurements of ϕ are made. The overall weighted RMS error is finally divided by the overall weighted RMS value of the quantity ϕ , and RMS errors are aggregated over both the water column depth and flow. The $MSS_{\Sigma,p}$ is also similarly computed, but here the overall weighted mean squared error is divided by the overall weighted mean squared potential error, $PE_{\phi,p}$, and the skill is equipartitioned between water column depth and flow. For simplicity, we chose $N_{\phi,i}$ simply as the number of stations in each region specified in Table 3 in the main paper. Rigorously, a specification is indicated in which the contribution of each location should be weighted by the number of locations within the range of the semivariogram associated with the river-course that location is within (Curran 1988).

5.3. Error Decomposition

The RMS error at a location can be decomposed into a systematic and an unsystematic part. If a model represents certain physical processes somewhat accurately, then it can be idealized as

$$\widehat{\phi}_M = \beta_0 + \beta_1 \phi_0 \quad (\text{A-5.6})$$

where β_0 and β_1 are regression parameters. The systematic component of error is then (Willmott 1981)

$$\varepsilon_{\phi,s} = \sqrt{\beta_0^2 + (\beta_1 - 1)^2 \frac{1}{N} \sum_{i=1}^N \phi_{0,i}^2 + 2\beta_0(\beta_1 - 1)E(\phi_0)} \quad (\text{A-5.7})$$

where $E(\phi_0)$ is the temporal mean of the observations. The unsystematic component of error is (Willmott 1981)

$$\varepsilon_{\phi,u} = \sqrt{\varepsilon_{\phi}^2 - \varepsilon_{\phi,s}^2} \quad (\text{A-5.8})$$

We discuss the implications of this error decomposition analysis in Section 5.

5.4 Comparison Metrics for Modeled and Observed Tidal Flows and Harmonic Components

The deviation of the modeled subtidal flow from that observed at a location can be succinctly represented by a target diagram (Jolliff et al. 2009; MacWilliams et al. 2015). In these diagrams, and are given by (MacWilliams et al. 2015),

$$\begin{aligned} \text{UBRMSD} &= \frac{\sqrt{\frac{1}{N} \sum_{i=1}^N \left[\left(\phi_{M,i} - \overline{\phi_M} \right) - \left(\phi_{0,i} - \overline{\phi_0} \right) \right]^2}}{\sigma_0} \frac{(\sigma_M - \sigma_0)}{|\sigma_M - \sigma_0|} \\ b &= \frac{\frac{1}{N} \sum_{i=1}^N \phi_{M,i} - \frac{1}{N} \sum_{i=1}^N \phi_{0,i}}{\sigma_0} \end{aligned} \quad (\text{A-5.9})$$

where $\overline{}$ denotes the grand mean over all N time-steps.

The deviation of the modeled harmonic components from those observed at a location can also be represented by a target diagram. A harmonic component's observed value is $f_0 = \zeta_0 \cos(\omega t + \psi_0)$, while the modeled component's value is $f_M = \zeta_M \cos(\omega t + \psi_M)$, so that after converting to polar coordinates, their fractional difference can be written as

$$\frac{f_M - f_O}{f_O} = \frac{(\zeta_M - \zeta_O)}{\zeta_O} e^{i\pi \left(\frac{\psi_M - \psi_O}{\pi} \right)} \quad (\text{A-5.10})$$

so that in Cartesian coordinates with the difference in amplitudes on the horizontal axis, and difference in phase on the vertical axis, the error between modeled and observed harmonic components can be succinctly represented by the point

$$\left(\frac{(\zeta_M - \zeta_O)}{\zeta_O}, \frac{\psi_M - \psi_O}{\pi} \right).$$

6. COMPREHENSIVE MODEL EVALUATION

We present the comprehensive results of our model evaluation for all model configurations subsequently. This section is a companion to the results and discussion presented in Sections 5 and 6.

6.1 DSM2 Model Valuation

Figure A-6.1 complements Figure 9 in the main paper, in which we show the error decomposition analysis for some model configurations.

Figures A-6.2 and A-6.3 complement Figures 18 and 19 in the main paper, where we show the target diagrams for some model configurations.

Figure A-6.4 complements Figure 20 in the main paper, in which we show the RMS error in hydrodynamic quantities as a function of inflow for some model configurations.

6.2 Patterns in Modeling the Hydrodynamic Quantities

In Figures 10–12 in the main paper, we show total instantaneous flow and water column depth, and daily averaged salinity at four representative locations. In companion Figures A-6.5 through A-6.7, we show these quantities for model configuration G1T60B1 at many more locations to provide a better coverage of the hydrodynamic landscape of the Delta. In Figure 13, we show spatial maps of the observed and modeled electrical conductivity for the G1T15B1 model configuration. In companion Figure A-6.8, we include the results of all the model configurations.

In Figures 14–16 in the main paper, we show spatial maps of some of the harmonically decomposed tidal components of water column depth and flow, and subtidal flow for the G1T15B1 model configuration. In the corresponding Figures A-6.9 to A-6.11, we show all these quantities for all model configurations.

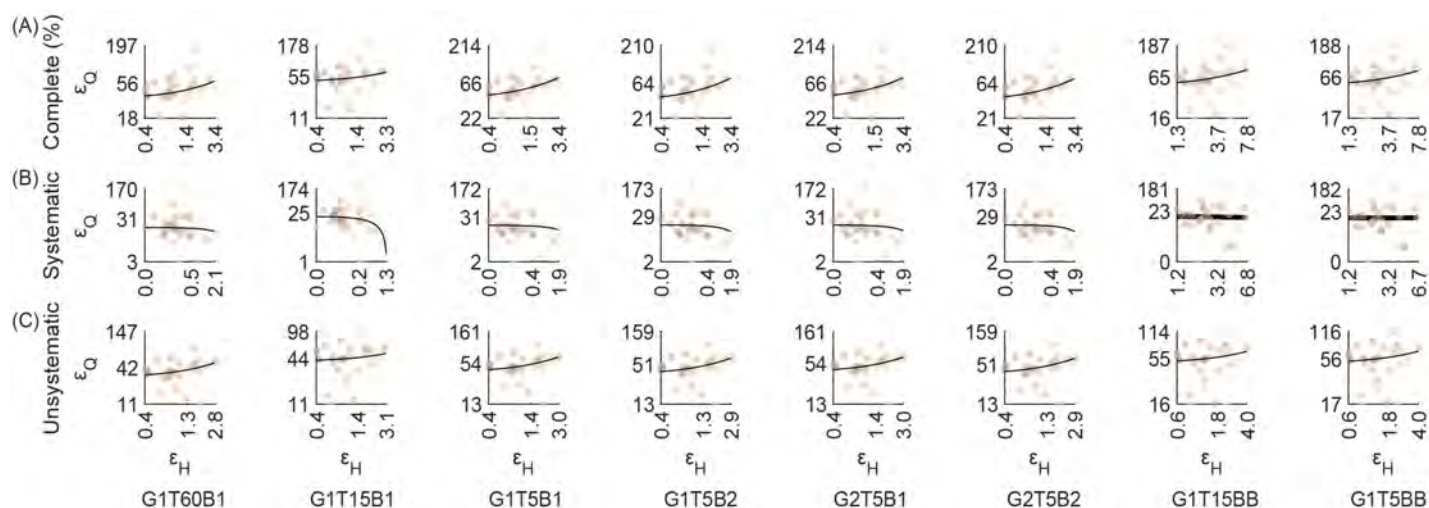


Figure A-6.1 Phase diagram errors in flow and depth for each location at which observations are available for all model configurations: (A–C) RMS error, (D–F) systematic or modeled component of RMS error, and (G–I) unsystematic or unrepresented physical processes induced component of RMS error. The scales are logarithmic, the points are color-coded by the distances of the locations at Martinez (landward points are lighter), and the Theil–Sen robust linear least squares (Ohlson and Kim 2015) lines are indicated. In (B), uncorrelated ε_H and ε_Q are indicated by thick lines.

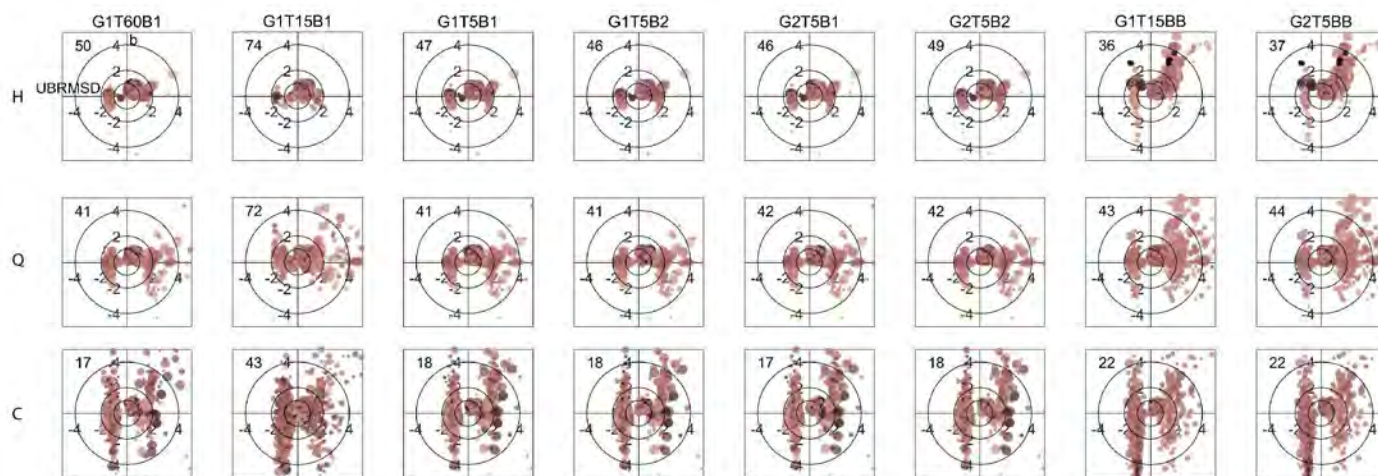


Figure A-6.2 Unbiased RMS difference and bias between model results and observations for all model configurations in instantaneous water column depth and flow, and daily averaged electrical conductivity. In each plot, the unbiased RMS difference is on the abscissa and the bias is on the ordinate axes, colors are lighter landward, and points are bigger with increasing total inflow into the system. Circles of dimensionless radii 1, 2, and 4 are indicated. The numbers indicate the percent of points that fall within the radius-1 circle. Note that the G1T15B1, G1T15BB and G2T5BB model configurations are favorably skewed by the wet years.

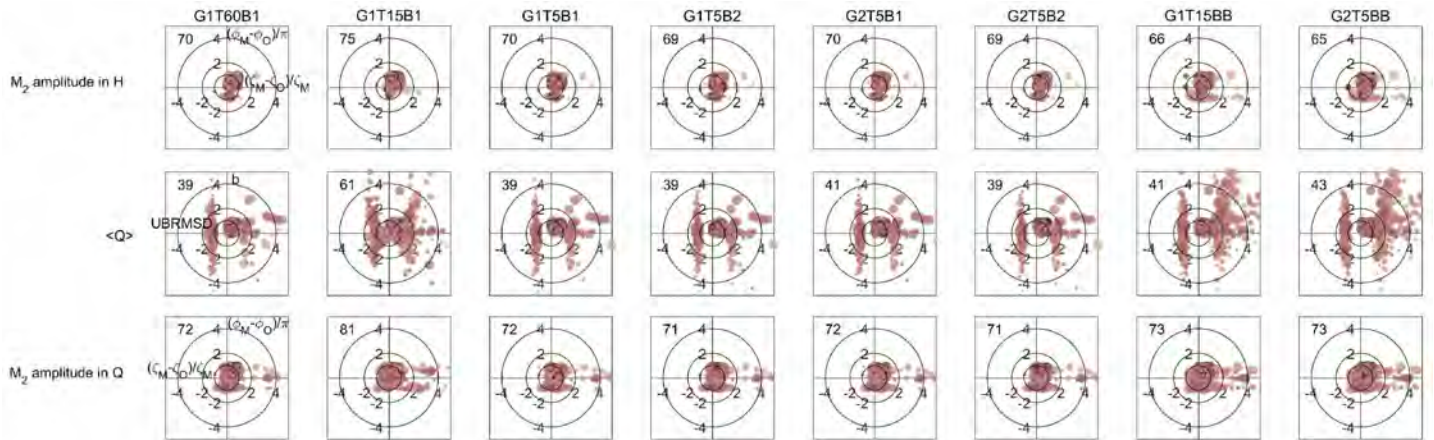


Figure A-6.3 Errors in amplitudes and phases of the M_2 component of water column depth and flow, and unbiased RMS difference and bias between model results and observations in the subtidal flow, for all model configurations. In each plot, the unbiased RMS difference or error in amplitudes is on the abscissa and the bias or error in phases is on the ordinate axes, colors are lighter landward, and points are bigger with increasing total inflow into the system. Circles of dimensionless radii 1, 2, and 4 are indicated. The numbers indicate the percent of points that fall within the radius-1 circle. Note that the G1T15B1, G1T15BB, and G2T5BB model configurations are favorably skewed by the wet years. We have jittered points with model predictions within the data precision inside the radius-1 circle for better readability.

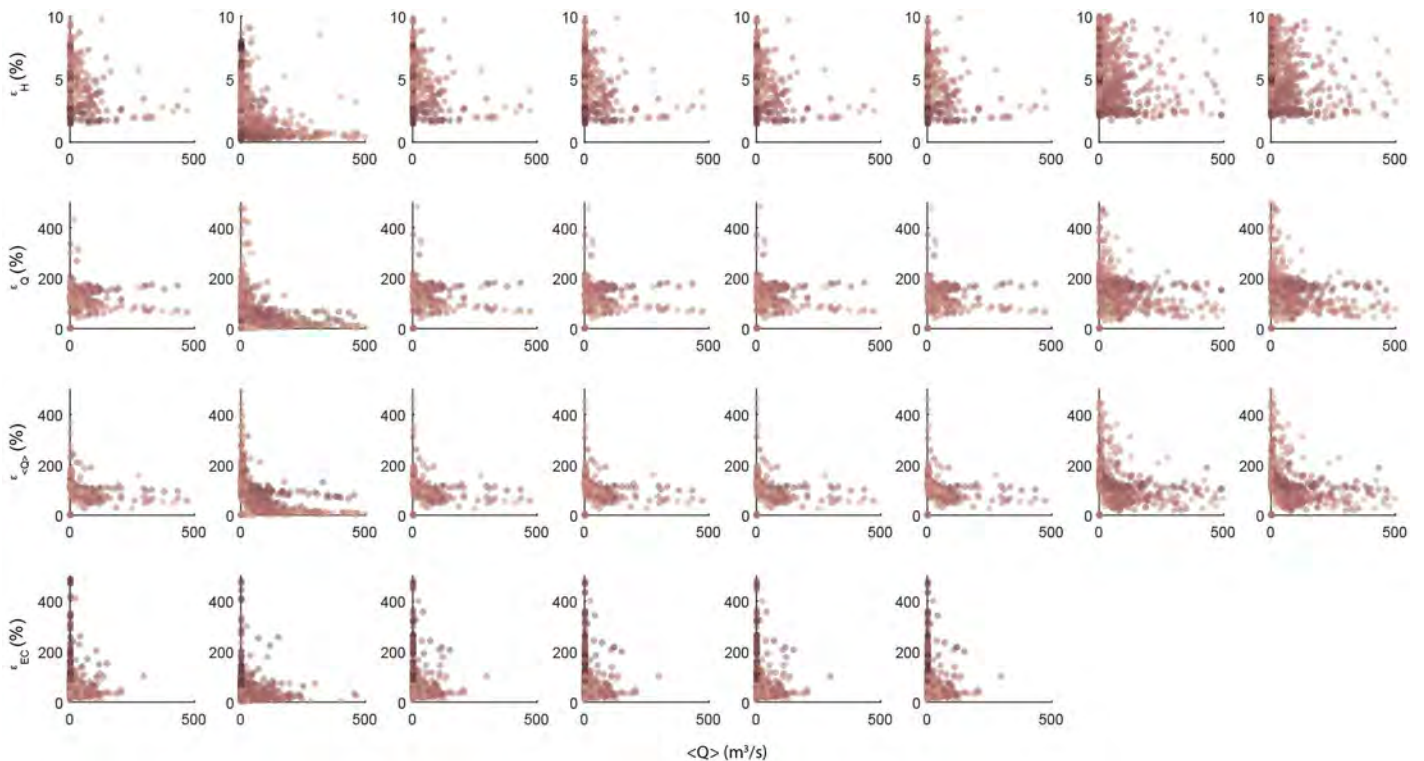


Figure A-6.4 RMS error in instantaneous water column depth and flow, subtidal flow, and daily averaged electrical conductivity as a fraction of the RMS values of these quantities versus the subtidal flow magnitude at various locations for all model configurations. In each plot, the colors are lighter landward. Note that the G1T15B1, G1T15BB, and G2T5BB model configurations are favorably skewed by the wet years.

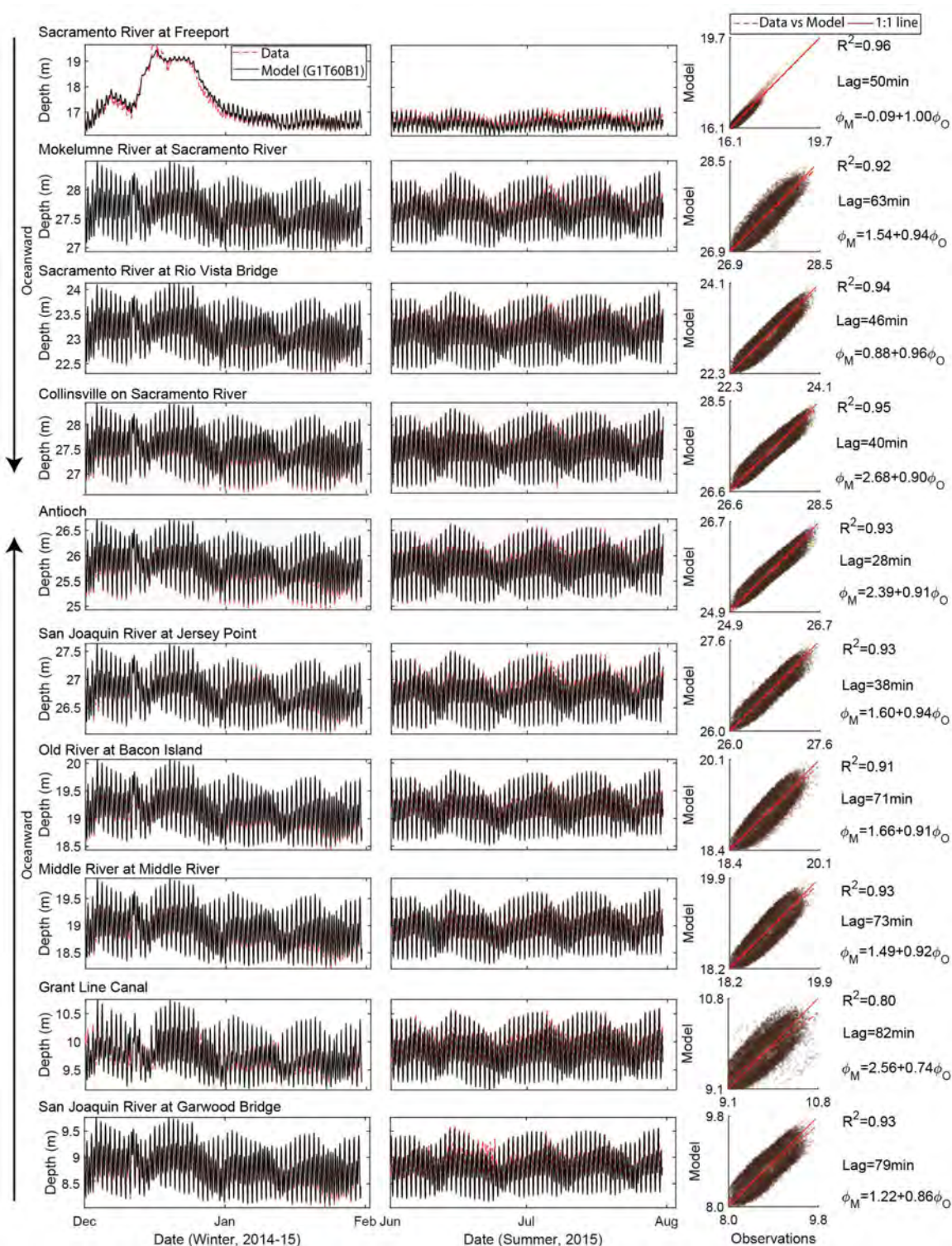


Figure A-6.5 Validation of DSM2 for instantaneous total water level at representative locations in the north and south Delta. For each location, a wet period (December 2014 to February 2015) and a dry period (June to August 2015) are compared. Scatter points are *color coded* by the instantaneous inflows (*light to dark* representing low to high flows) into the system. The 1:1 correspondence, linear regression of the phase-corrected model results with the observations, the correlation coefficient, and lag are indicated. In all the plots, the model configuration, G1T60B1, with least overall RMS error is represented.

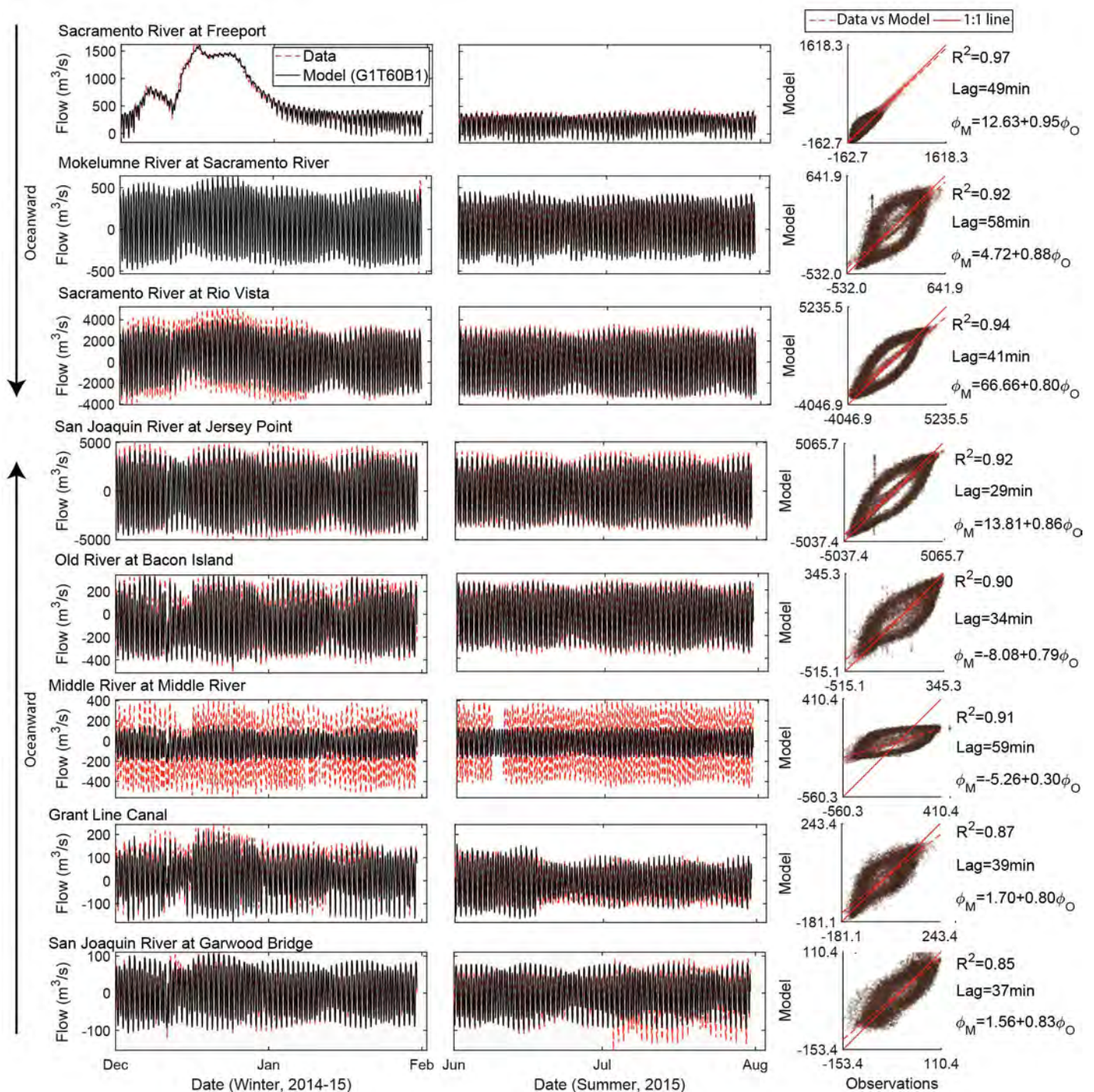


Figure A-6.6 Validation of DSM2 for instantaneous total flow at representative locations in the north and south Delta. For each location, a wet period (December 2014 to February 2015) and a dry period (Jun to Aug 2015) are compared. The tidal effects are poorly represented in the Middle River at the “Middle River at Middle River” location, causing the low fidelity here. Scatter points are *color coded* by the instantaneous inflows (*light to dark* representing low to high flows) into the system. The 1:1 correspondence, linear regression of the phase-corrected model results with the observations, the correlation coefficient, and lag are indicated. In all the plots, the model configuration, G1T60B1, with least overall RMS error is represented.

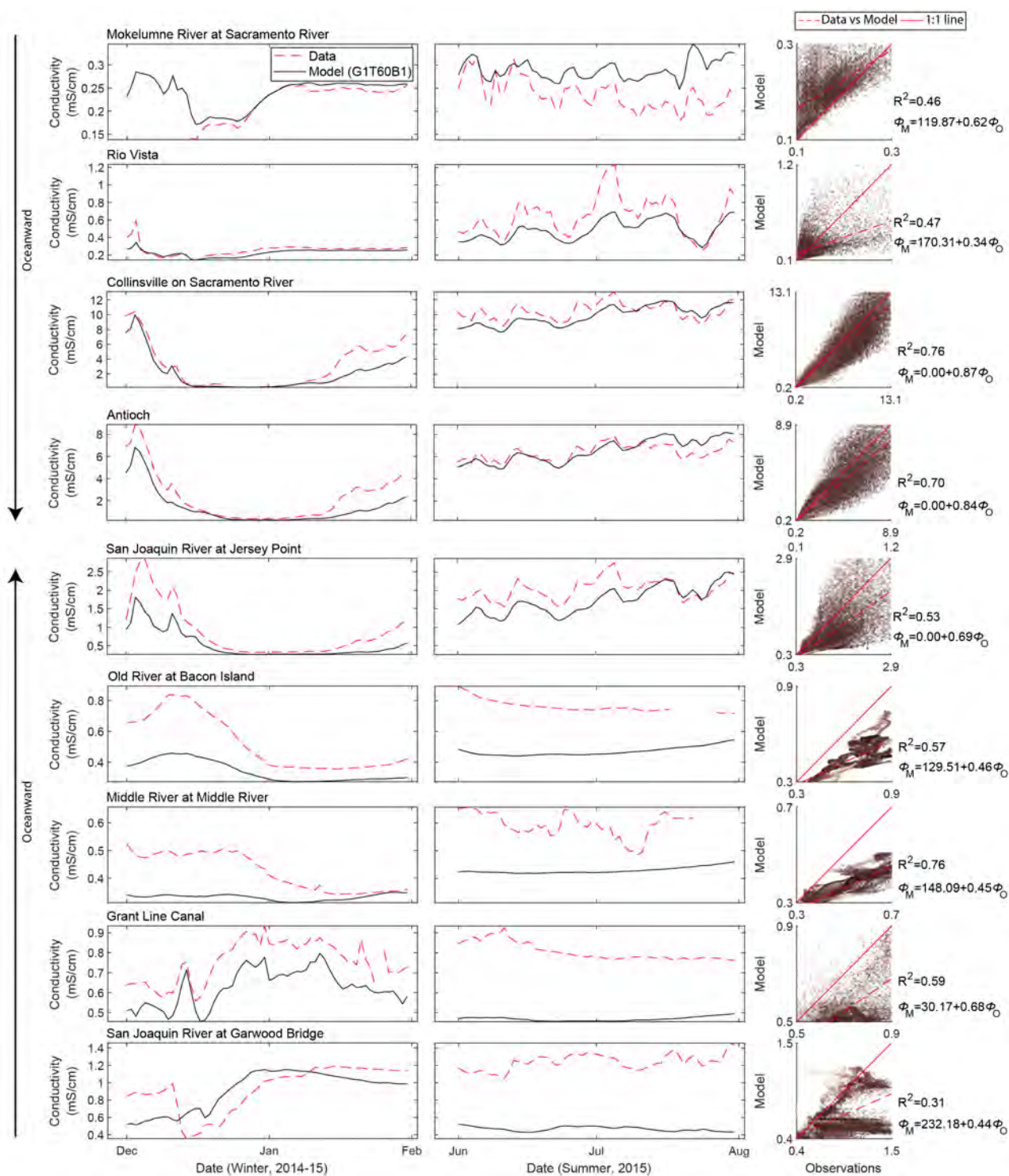


Figure A-6.7 Validation of DSM2 for daily averaged electrical conductivity at representative locations in the north and south Delta. For each location, a wet period (December 2014 to February 2015) and a dry period (June to August 2015) are compared. Scatter points are color coded by the instantaneous inflows (light to dark representing low to high flows) into the system. The 1:1 correspondence, linear regression of the phase-corrected model results with the observations, the correlation coefficient, and lag are indicated. In all the plots, the model configuration, G1T60B1, with least overall RMS error is represented.

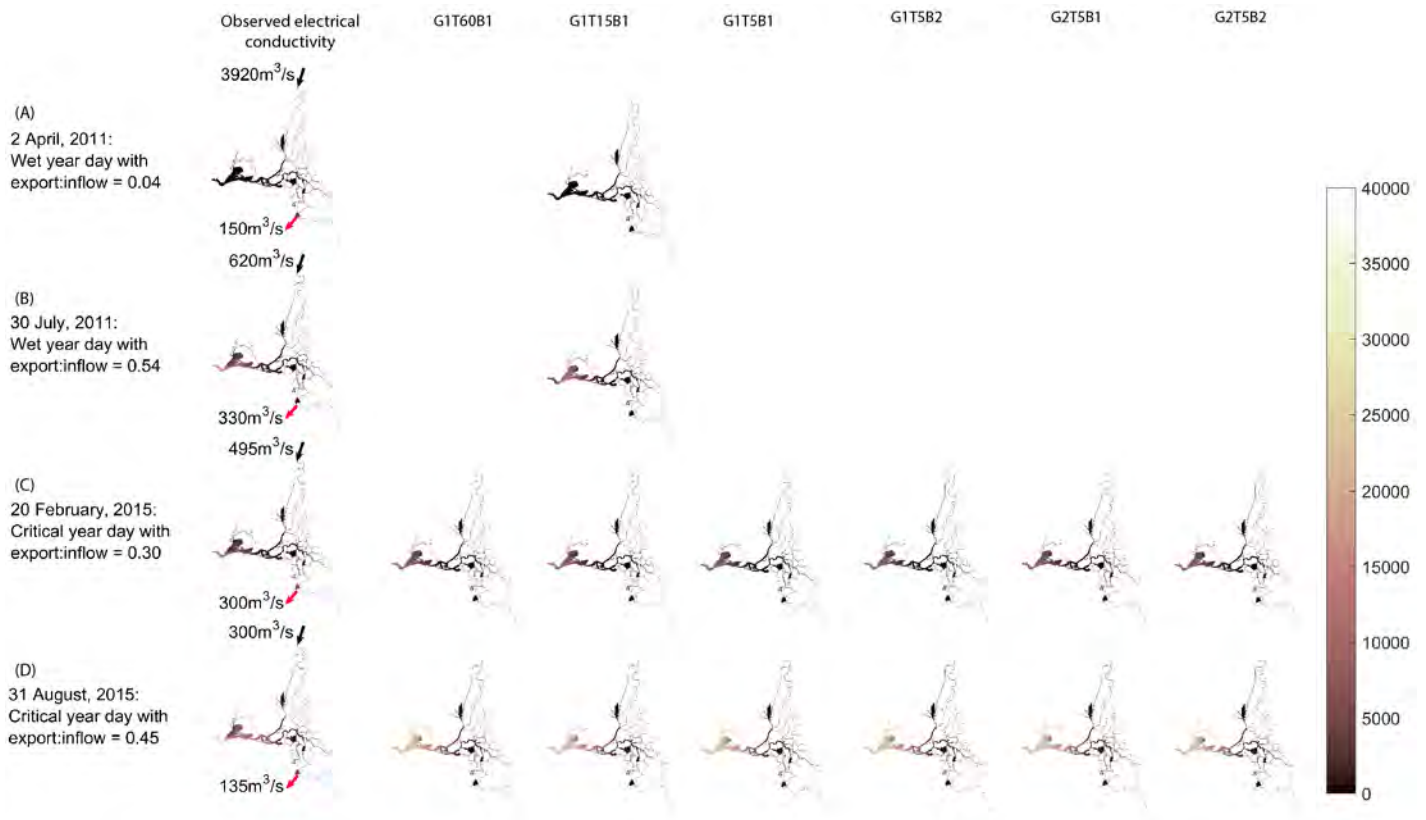


Figure A-6.8 Observed and modeled daily averaged electrical conductivities for a representative day in various hydrologic and water operations scenarios: **(A)** wet year with a small export flow to inflow ratio, **(B)** wet year with a large export flow to inflow ratio, **(C)** critically dry year with a typical export flow to inflow ratio, and **(D)** critically dry year with a large export flow to inflow ratio. In the maps on the *left*, electrical conductivity measured at different locations is bilinearly interpolated over the entire domain. In the maps on the *right*, bilinearly-interpolated observations are subtracted from bilinearly-interpolated modeled electrical conductivities. In each figure, the average inflow and export flow in that day is indicated by *arrows* on the Sacramento River and near the pumps, respectively.



Figure A-6.9 Observed and modeled average tidal decomposition of water column depth in the summer of a critically dry year (July to September, 2015, with an average daily inflow of $275 \text{ m}^3 \text{ s}^{-1}$ and an average export:inflow ratio of 0.15): tidal harmonic component amplitudes for K_1 , M_2 , MK_3 , and M_4 , and range in the spring–neap cycle. In each figure, the *gray levels* indicate the water column depth, and the *pink levels* indicate the tidal phase. The *scale bars* apply to both the top and bottom maps. Note that we have not reported the phase of the spring–neap oscillation, because the difference in tidal range was not estimated through harmonic analysis.

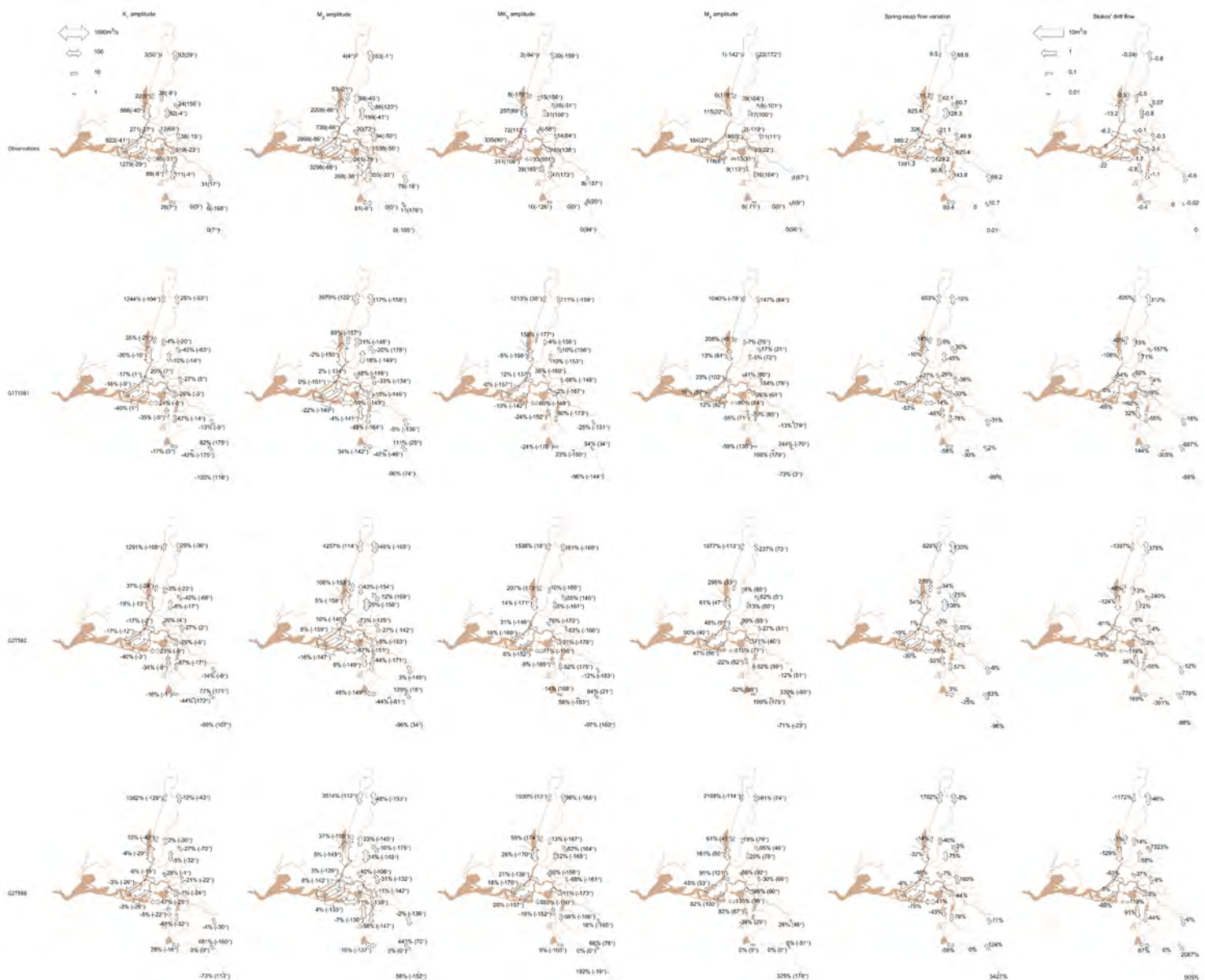


Figure A-6.10 Observed and modeled tidal components of flow in a critically dry year (July to September, 2015, average daily inflow = $275 \text{ m}^3 \text{ s}^{-1}$ and average export:inflow ratio = 0.15): K_1 , M_2 , MK_3 , and M_4 harmonic components, spring–neap cycle range, and Stokes' drift. In the *top row*, *arrows sizes* correspond to observed amplitudes, and the amplitudes and Greenwich phases (*within parentheses*) are indicated. In *subsequent rows*, *arrows sizes* correspond to modeled amplitudes, and values indicate percentage differences between the modeled and observed amplitudes, and absolute difference in the Greenwich phase (within parentheses). *Arrows* are sized on a logistic scale, and the scaling is different for the Stokes' drift than for the other parts of the tidal flow because it is very small in comparison with the tidal harmonic amplitudes.

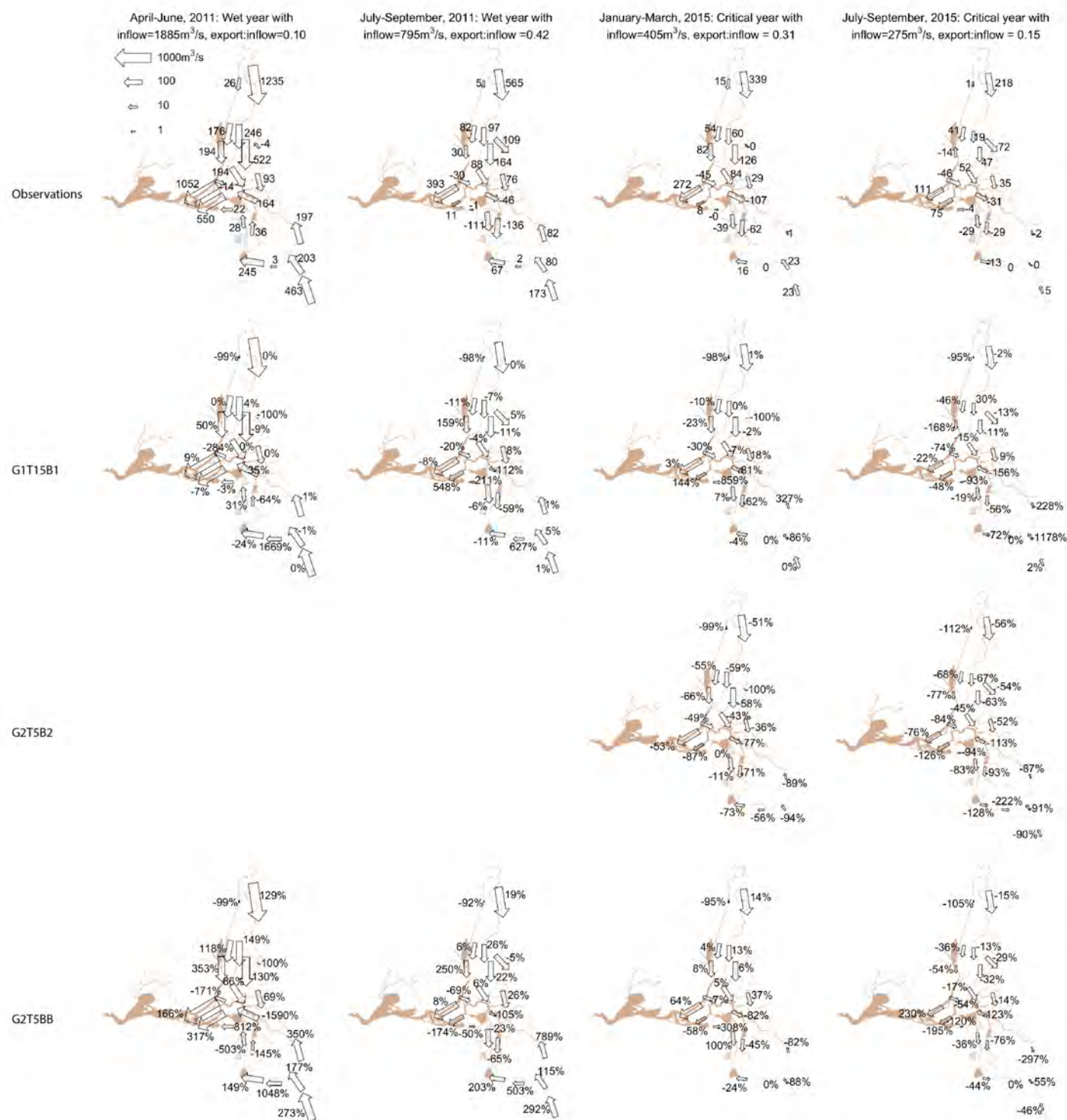


Figure A-6.11 Observed and modeled average subtidal flow and Stokes' drift in the spring in a wet year, summer in a wet year, winter in a critically dry year, and summer in a critically dry year. In each season, the average daily inflow and the ratio of total export flows to total inflow are indicated. The first two seasons are not available in certain runs because of the durations of the runs. In the *top row*, *arrows sizes* correspond to observed flows, which are indicated. In *subsequent rows*, *arrows sizes* correspond to modeled flows, and values indicate percentage differences between the modeled and observed flows. Arrows are sized on a logistic scale.

REFERENCES

- Aubrey DG, Speer PE. 1984. A study of non-linear tidal propagation in shallow inlet/estuarine systems part I: observations. *Estuary Coast Shelf Sci* [Internet]. [cited 2017 April 6];21:185–205. Available from: <http://www.sciencedirect.com/oca.ucsc.edu/science/article/pii/0272771485900964>
[https://doi.org/10.1016/0272-7714\(85\)90096-4](https://doi.org/10.1016/0272-7714(85)90096-4)
- BDO: Bay Delta Office [Internet]. c2002. Sacramento (CA): DSM2 grid version 2.0; [updated 2013 November 1; cited 2017 April 6]. Available from: http://baydeltaoffice.water.ca.gov/modeling/deltamodeling/models/DSM2v6/DSM2_Grid2.0.pdf
- Becherer J, Flöser G, Umlauf L, Burchard H. 2016. Estuarine circulation versus tidal pumping: Sediment transport in a well-mixed tidal inlet. *J Geophys Res Oceans* [Internet]. [cited 2018 February 1];121(8):6251–6270. Available from: <http://onlinelibrary.wiley.com/doi/10.1002/2016JC011640/full>
<https://doi.org/10.1002/2016JC011640>
- Braca G. 2008. FORALPS: Stage-discharge relationships in open channels: practices and problems. Trento (Italy): Università degli Studi di Trento, Dipartimento di Ingegneria Civile e Ambientale. Technical Report 11. 24 p.
- Calmant S, Seyler F. 2006. Continental surface waters from satellite altimetry. *Comptes Rendus Geosci* [Internet]. [cited 2018 May 7];338(14–15):1113–1122. Available from: <https://www.sciencedirect.com/science/article/pii/S1631071306001210>
<https://doi.org/10.1016/j.crte.2006.05.012>
- CDEC: California Data Exchange Center [Internet]. c2016. Sacramento (CA): USGS flow and stage data; [updated 2017 April 6; cited 2017 April 6]. Available from: <http://cdec.water.ca.gov/>
- Cornish CR, Bretherton CS, Percival DB. 2006. Maximal overlap wavelet statistical analysis with application to atmospheric turbulence. *Boundary-Layer Meteorol* [Internet]. [cited 2018 February 6];119(2), 339–374. Available from: <https://link.springer.com/article/10.1007/s10546-005-9011-y>
<https://doi.org/10.1007/s10546-005-9011-y>
- Csanady GT. 1973a. Wind-induced barotropic motions in long lakes. *J Phys Oceanogr* [Internet]. [cited 2018 January 25];3(4):429–438. Available from: [https://journals.ametsoc.org/doi/abs/10.1175/1520-0485\(1973\)003%3C0429:WIBMIL%3E2.0.CO%3B2](https://journals.ametsoc.org/doi/abs/10.1175/1520-0485(1973)003%3C0429:WIBMIL%3E2.0.CO%3B2)
[https://doi.org/10.1175/1520-0485\(1973\)003<0429:WIBMIL>2.0.CO;2](https://doi.org/10.1175/1520-0485(1973)003<0429:WIBMIL>2.0.CO;2)
- Csanady GT. 1973b. Wind-induced baroclinic motions at the edge of the continental shelf. *J Phys Oceanogr* [Internet]. [cited 2018 January 25];3(3):274–279. Available from: [https://journals.ametsoc.org/doi/abs/10.1175/1520-0485\(1973\)003%3C0274%3AWBMATE%3E2.0.CO%3B2](https://journals.ametsoc.org/doi/abs/10.1175/1520-0485(1973)003%3C0274%3AWBMATE%3E2.0.CO%3B2)
[https://doi.org/10.1175/1520-0485\(1973\)003<0274:WBMATE>2.0.CO;2](https://doi.org/10.1175/1520-0485(1973)003<0274:WBMATE>2.0.CO;2)
- Curran PJ. 1988. The semivariogram in remote sensing: an introduction. *Remote Sens Environ*. 1988 [Internet]. [cited 2018 February 7];24(3):493–507. Available from: <https://www.sciencedirect.com/science/article/pii/0034425788900211>
[https://doi.org/10.1016/0034-4257\(88\)90021-1](https://doi.org/10.1016/0034-4257(88)90021-1)
- Dugge J. [Internet]. c2015. xy2sn; [updated 2015 August 2015; cited 2018 January 26]. Available from: <https://www.mathworks.com/matlabcentral/fileexchange/39796-jdugge-xy2sn>
- Finch R, Enright C, Rayej M. 2001. Cross Section Development Program CSDP Version 2.4d. Sacramento (CA): Department of Water Resources. User's Manual [Internet]. [cited 2018 January 26]; 33 p. Available from: <http://baydeltaoffice.water.ca.gov/modeling/deltamodeling/models/csdp/csdpmanual.pdf>
- Fischer HB, List EJ, Koh RCY, Imberger J, Brooks NH. 1979. Mixing in inland and coastal waters. New York (NY): Academic Press. p. 1–483.
- Furniss M, Love M, Firor S, Moynan K, Llanos A, Guntle J, Gubernick R. 2006. FishXing, version 3.0. San Dimas (CA): United States Forest Service User Manual and Reference [Internet]. [cited 2018 January 30]; 231 p. Available from: http://www.fsl.orst.edu/geowater/FX3/FX3_manual.pdf

- Geyer WR, MacCready P. 2014. The estuarine circulation. *Annu Rev Fluid Mech* [Internet]. [cited 2018 January 22];46:175–197. Available from: <http://www.annualreviews.org/doi/full/10.1146/annurev-fluid-010313-141302>
<https://doi.org/10.1146/annurev-fluid-010313-141302>
- Geyer WR, Signell RP. 1992. A reassessment of the role of tidal dispersion in estuaries and bays. *Estuary Coasts* [Internet]. [cited 2018 January 22];15(2):97–108. Available from: <https://link.springer.com/article/10.2307%2F1352684?LI=true>
<https://doi.org/10.2307/1352684>
- Gleichenhauf KT, Wolfram PJ, Monsen NE, Fringer OB, Monismith SG. 2014. Dispersion mechanisms of a tidal river junction in the Sacramento-San Joaquin Delta, California. *San Franc Estuary Watershed Sci* [Internet]. [cited 2017 April 7];12(4). Available from: <https://escholarship.org/uc/item/6js9z7bc>
<https://doi.org/10.15447/sfews.2014v12iss4art1>
- Ivey GN, Winters KB, Koseff JR. 2008. Density stratification, turbulence, but how much mixing? *Annu Rev Fluid Mech* [Internet]. [cited: 2018 January 22];40:169–184. Available from: <http://centerforoceansolutions.org/sites/default/files/publications/Ivey%20et%20al%202008-Density.pdf>
<https://doi.org/10.1146/annurev-fluid.39.050905.110314>
- Jay DA, Uncles RJ, Largeir J, Geyer WR, Vallino J, and Boynton WR. 1997. A review of recent developments in estuarine scalar flux estimation. *Estuary Coasts* [Internet]. [cited: 2018 January 23]; 20(2):262–280. Available from: <https://link.springer.com/article/10.2307/1352342>
<https://doi.org/10.2307/1352342>
- Jolliff JK, Kindle JC, Shulman I, Penta B, Friedrichs MA, Helber R, Arnone RA. 2009. Summary diagrams for coupled hydrodynamic-ecosystem model skill assessment. *J Mar Sys* [Internet]. [cited: 6 February 2018];76(1-2):64–82. Available from: <https://www.sciencedirect.com/science/article/pii/S0924796308001140>
<https://doi.org/10.1016/j.jmarsys.2008.05.014>
- Kirgöz MS. 1989. Turbulent velocity profiles for smooth and rough open channel flow. *J Hydraul Engr* [Internet]. [cited 2017 April 7];115(11):1543–1561. Available from: [http://ascelibrary.org/doi/abs/10.1061/\(ASCE\)0733-9429\(1989\)115:11\(1543\)](http://ascelibrary.org/doi/abs/10.1061/(ASCE)0733-9429(1989)115:11(1543))
[https://doi.org/10.1061/\(ASCE\)0733-9429\(1989\)115:11\(1543\)#sthash.Etau9k2i.dpuf](https://doi.org/10.1061/(ASCE)0733-9429(1989)115:11(1543)#sthash.Etau9k2i.dpuf)
- Longuet-Higgins M. 1969. On the transport of mass by time-varying ocean currents. *Deep Sea Res* [Internet]. [cited 2017 April 7];16:431–447. Available from: <http://www.sciencedirect.com/science/article/pii/001174716990031X>
[https://doi.org/10.1016/0011-7471\(69\)90031-X](https://doi.org/10.1016/0011-7471(69)90031-X)
- MacCready P. 1999. Estuarine adjustment to changes in river flow and tidal mixing. *J Phys Oceanogr* [Internet]. [cited 2018 March 14]; 29(4):708–726. Available from: [https://journals.ametsoc.org/doi/full/10.1175/1520-0485\(1999\)029%3C0708:EATCIR%3E2.0.CO%3B2](https://journals.ametsoc.org/doi/full/10.1175/1520-0485(1999)029%3C0708:EATCIR%3E2.0.CO%3B2)
[https://doi.org/10.1175/1520-0485\(1999\)029<0708:EATCIR>2.0.CO;2](https://doi.org/10.1175/1520-0485(1999)029<0708:EATCIR>2.0.CO;2)
- MacCready P, Geyer WR. 2010. Advances in estuarine physics. *Annu Rev Mar Sci* [Internet]. [cited: 2018 January 23];2:35–58. Available from: <http://www.annualreviews.org/doi/full/10.1146/annurev-marine-120308-081015>
<https://doi.org/10.1146/annurev-marine-120308-081015>
- MacWilliams ML, Bever AJ, Gross ES, Ketefian GS, Kimmerer WJ. 2015. Three-dimensional modeling of hydrodynamics and salinity in the San Francisco estuary: An evaluation of model accuracy, X2, and the low-salinity zone. *San Franc Estuary Watershed Sci* [Internet]. [cited 2017 July 14];13(1). Available from: <http://escholarship.org/uc/item/7x65r0tf>
<https://doi.org/10.15447/sfews.2015v13iss1art2>
- MacWilliams ML, Gross ES, DeGeorge JF, Rachielle RR. 2007. Three-dimensional hydrodynamic modeling of the San Francisco Estuary on an unstructured grid. *Proceedings of the International Association for Hydraulic Research* (Vol. 16); 2007; Venice (Italy). p. 1–11.

- Merwade VM, Maidment DR, Hodges BR. 2005. Geospatial representation of river channels. *J Hydrol Engr* [Internet]. [cited 2018 January 26];10(3):243–251. Available from: [https://ascelibrary.org/doi/abs/10.1061/\(ASCE\)1084-0699\(2005\)10:3\(243\)https://doi.org/10.1061/\(ASCE\)1084-0699\(2005\)10:3\(243\)](https://ascelibrary.org/doi/abs/10.1061/(ASCE)1084-0699(2005)10:3(243)https://doi.org/10.1061/(ASCE)1084-0699(2005)10:3(243))
- Monismith SG. 2016. A note on Delta Outflow. *San Franc Estuary Watershed Sci* [Internet]. [cited 2017 April 7];14(3). Available from: http://escholarship.org/uc/item/89k7b61mhttps://doi.org/10.15447/sfews_2016v14iss3art3
- Monismith SG, Hensch JL, Fong DA, Nidzieko NJ, Fleenor WE, Doyle LP, Schadow SG. 2009. Thermal variability in a tidal river. *Estuary Coasts* [Internet]. [cited 2017 April 7];32:100–110. Available from: <https://link.springer.com/article/10.1007/s12237-008-9109-9https://doi.org/10.1007/s12237-008-9109-9>
- Monismith SG, Kimmerer W, Burau JR, Stacey MT. 2002. Structure and flow-induced variability of the subtidal salinity field in northern San Francisco Bay. *J Phys Oceanogr* [Internet]. [cited 2017 April 7];32(11):3003–3019. Available from: [http://journals.ametsoc.org/doi/abs/10.1175/1520-0485\(2002\)032%3C3003:SAFIVO%3E2.0.CO%3B2http://doi.org/10.1175/1520-0485\(2002\)032%3C3003:SAFIVO%3E2.0.CO%3B2](http://journals.ametsoc.org/doi/abs/10.1175/1520-0485(2002)032%3C3003:SAFIVO%3E2.0.CO%3B2http://doi.org/10.1175/1520-0485(2002)032%3C3003:SAFIVO%3E2.0.CO%3B2)
- Muste M, Yu K, Spasojevic M. 2004. Practical aspects of ADCP data use for quantification of mean river flow characteristics; Part I: moving-vessel measurements. *Flow Meas Instr* [Internet]. [cited 2017 April 7];15:1–16. Available from: <http://www.sciencedirect.com/science/article/pii/S0955598603000670https://doi.org/10.1016/j.flowmeasinst.2003.09.001>
- Nidzieko, N.J. 2010. Tidal asymmetry in estuaries with mixed semidiurnal/diurnal tides. *J Geophys Res: Ocean* [Internet]. [cited 2018 May 7];115(C8). Available from: <https://agupubs.onlinelibrary.wiley.com/doi/full/10.1029/2009JC005864https://doi.org/10.1029/2009JC005864>
- NOAA-TC: National Oceanic and Atmospheric Administration – Tides and Currents [Internet]. c2013. Silver Spring (MD): Observed water levels at Martinez Amorco Pier, California; [updated 2018 January 21; cited 2018 January 21]. Available from: <https://tidesandcurrents.noaa.gov/stationhome.html?id=9415102>
- Okubo A. 1973. Effect of shoreline irregularities on streamwise dispersion in estuaries and other embayments. *Netherlands J Sea Res* [Internet]. [cited 2018 May 7];6(1-2):213–224. Available from: [https://www.sciencedirect.com/science/article/pii/0077757973900148https://doi.org/10.1016/0077-7579\(73\)90014-8](https://www.sciencedirect.com/science/article/pii/0077757973900148https://doi.org/10.1016/0077-7579(73)90014-8)
- Onset: Onset Computer Corporation. 2017. HOBO U24 conductivity logger (U24-002-C) manual. Bourne (MA): User Manual [Internet]. [cited 2018 January 21]; 6 p. Available from: http://www.onsetcomp.com/files/manual_pdfs/16844-D%20MAN-U24-002-C.pdf
- Park J, Heitsenrether R, Sweet, WV. 2014. NOAA: Water level and wave height estimates at NOAA tide stations from acoustic and microwave sensors. Silver Spring (MA): NOAA Center for Operational Oceanographic Products and Services, National Ocean Service Technical Report NOS CO-OPS 075 [Internet]. [cited 2017 April 7]; 50 p. Available from: https://tidesandcurrents.noaa.gov/publications/NOAA_Tech_075_Microwave_Water_Level_2014_Final.pdf
- Patel AX, Kundu P, Rubinov M, Jones PS, Vértés PE, Ersche KD, Suckling J, Bullmore ET. 2014. A wavelet method for modeling and despiking motion artifacts from resting-state fMRI time series. *Neuroimage* [Internet]. [cited 2018 February 6];95:287–304. Available from: <https://www.sciencedirect.com/science/article/pii/S1053811914001578https://doi.org/10.1016/j.neuroimage.2014.03.012>
- QGIS Development Team. 2016. Beaverton (OR): QGIS Geographic Information System. Open Source Geospatial Foundation Project.
- Ralston DK, Stacey MT. 2005. Longitudinal dispersion and lateral circulation in the intertidal zone. *J Geophys Res: Oceans*. [Internet]. [cited 2018 January 30]; 110(C7):C0715. Available from: <http://onlinelibrary.wiley.com/doi/10.1029/2005JC002888/fullhttps://doi.org/10.1029/2005JC002888>
- Ridderinkhof H, Zimmerman JT. 1992. Chaotic stirring in a tidal system. *Sci* [Internet]. [cited 2018 February 1];258(5085):1107–1111. Available from: <http://science.sciencemag.org/content/258/5085/1107https://doi.org/10.1126/science.258.5085.1107>

- RTC: Romburg Tiburon Center [Internet]. c2017. Tiburon (CA): Carquinez strait buoy data; [updated 2017 October 30; cited 2017 October 30]. Available from: <https://coastwatch.pfeg.noaa.gov/erddap/tabledap/rtcctdCMAysi.mat?time%2Cdepth&time%3E=2009-01-01T00%3A00%3A00Z&time%3C=2016-01-01T00%3A00%3A00Z>
- Sassi MG, Hoitink AJF, de Brye B, Vermuelen B, Deleersnijder E. 2011. Tidal impact on the division of river discharge over distributary channels in the Mahakam Delta. *Ocean Dyn* [Internet]. [cited 2017 April 7];61(12):2211–2228. Available from: <https://link.springer.com/article/10.1007/s10236-011-0473-9> <https://doi.org/10.1007/s10236-011-0473-9>
- Schemel LE. 2001. Simplified conversions between specific conductance and salinity units for use with data from monitoring stations. *Interagency Ecol Prog Newsletter* [Internet]. [cited 2018 January 31];14(1):17–18. Available from: <https://pubs.er.usgs.gov/publication/70174311>
- Signell RP, Beardsley RC, Graber HC, Capotondi A. 1990. Effect of wave-current interaction on wind-driven circulation in narrow, shallow embayments. *J Geophys Res Ocean* [Internet]. [cited: 2018 January 22];95(C6):9671–9678. Available from: <http://onlinelibrary.wiley.com/doi/10.1029/JC095iC06p09671/abstract> <https://doi.org/10.1029/JC095iC06p09671>
- Smith NP, Stoner AW. 1993. Computer simulations of larval transport through tidal channels: role of vertical migration. *Estuary Coast Shelf Sci* [Internet]. [cited 2017 April 7];37:43–58. Available from: <http://www.sciencedirect.com/science/article/pii/S0272771483710401> <https://doi.org/10.1006/ecss.1993.1040>
- Speer PE, Aubrey DG. 1984. A study of non-linear tidal propagation in shallow inlet/estuarine systems part II: theory. *Estuary Coast Shelf Sci* [Internet]. [cited 2017 April 7];21:207–224. Available from: <http://www.sciencedirect.com/science/article/pii/0272771485900976> [https://doi.org/10.1016/0272-7714\(85\)90097-6](https://doi.org/10.1016/0272-7714(85)90097-6)
- Sridharan VK. 2015. Scalar transport in channel networks: development of a particle tracking model to study the movement of scalars in the Sacramento-San Joaquin Delta [dissertation]. [Stanford (CA)]: Stanford University. p. 1–413.
- Sridharan VK, Monismith SG, Fong DA, Hench JL. 2018. One-dimensional particle tracking with streamline preserving junctions for flows in channel networks. *J Hydraul Engr* [Internet]. [cited 2018 February 1];144(2):04017063. Available from: [https://ascelibrary.org/doi/abs/10.1061/\(ASCE\)HY.1943-7900.0001399](https://ascelibrary.org/doi/abs/10.1061/(ASCE)HY.1943-7900.0001399) [https://doi.org/10.1061/\(ASCE\)HY.1943-7900.0001399](https://doi.org/10.1061/(ASCE)HY.1943-7900.0001399)
- USGS: United States Geological Survey [Internet]. c2016. Washington D.C.: How streamflow is measured part I: measuring stream stage; [updated 2016 December 9; cited 2017 April 7]. Available from: <https://water.usgs.gov/edu/streamflow1.html>
- Wang R, Ateljevich E. 2012. A continuous surface elevation map for modeling. In: Bay-Delta Office. 2012. Methodology for flow and salinity estimates in the Sacramento-San Joaquin Delta and Suisun Marsh. Sacramento (CA): California Department of Water Resources, Office of State Water Project Planning, Modeling Support Branch, Delta Modeling Section. Thirty-second Annual Progress Report to the State Water Resources Control Board. p. 121–146.
- Willmott CJ. 1981. On the validation of models. *Phys Geograph* [Internet]. [cited 2018 February 11];2(2):184–94. Available from: <http://www.tandfonline.com/doi/abs/10.1080/02723646.1981.10642213> <https://doi.org/10.1080/02723646.1981.10642213>
- Woodworth PL, Blackman DL, Pugh DT, Vassie JM. 2005. On the role of diurnal tides in contributing to asymmetries in tidal probability distribution functions in areas of predominantly semi-diurnal tide. *Estuary Coast Shelf Sci* [Internet]. [cited 2017 April 7];64:235–240. Available from: <http://www.sciencedirect.com/science/article/pii/S0272771405000557> <https://doi.org/10.1016/j.ecss.2005.02.014>

NOTES

Sridharan VK. 2018. Matlab toolbox for automatic clean-up of coastal and estuarine tidal datasets. Presented at: Delta Modeling Section Users Group Meeting; Sacramento, CA.